Chapter 8
Aspects of the Fractional Quantum Hall Effect in Graphene

Tapash Chakraborty and Vadim Apalkov

Abstract We present a brief overview of the nature of the fractional quantum Hall effect (FQHE) in monolayer and bilayer graphene. After a short introduction on the effect and the pseudopotential description of interacting electrons in the quantum Hall regime, we discuss in detail the magnetic field effects on electrons in monolayer graphene. We also briefly discuss the experimental signatures of the effect reported in the literature. In bilayer graphene, the effect manifests itself in a very different manner and we discuss in detail the various novel effects one expects there due to electron-electron interactions. The nature of the collective excitations of Dirac fermions in trilayer graphene is also briefly discussed. Existence of some exotic states in bilayer graphene, such as the Pfaffian state is also highlighted. Finally, we have touched upon the properties of the FQHE states of Dirac fermions on the surface of a topological insulator.

8.1 A Brief History of the Fractional Quantum Hall Effect

The quantum Hall effects (QHEs), both the integral [1, 2] and fractional [3, 4] QHEs are undoubtedly two of the most spectacular discoveries of the past century that have enormously enriched the field of condensed matter physics. Similarly, the theoretical explanation of the fractional QHE (FQHE) by Laughlin [5, 6] was a brilliant contribution to the annals of many-body physics. The experimental observation of the QHEs is summarized in Fig. 8.1. A two-dimensional electron gas in ultra-pure semiconductor materials, subjected to a high magnetic field and very low temperatures, i.e., in the extreme quantum limit, exhibits nearly vanishing longitudinal conductivity, $\sigma_{xx} \rightarrow 0$ and formation of steps in the Hall conductance

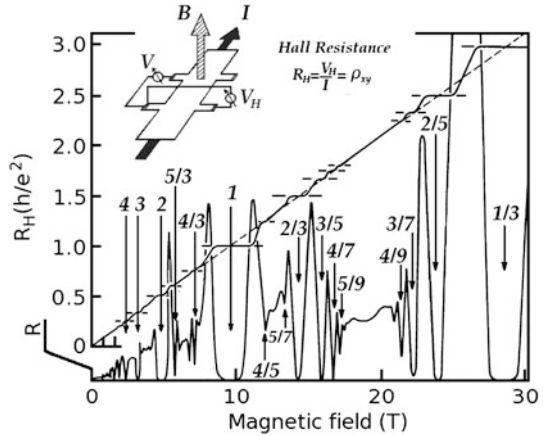$$\sigma_{xy} = \nu \frac{e^2}{h},$$

T. Chakraborty (✉)
Department of Physics and Astronomy, University of Manitoba, Winnipeg, Canada R3T 2N2
e-mail: Tapash.Chakraborty@umanitoba.ca

V. Apalkov
Department of Physics and Astronomy, Georgia State University, Atlanta, GA 30303, USA

Fig. 8.1 Fractional (and integer) filling factors where the QHE is observed (adopted from [71])

for special values of the quantum number ν. The *filling factor* ν is a simple integer for the IQHE, and a rational fraction $\nu = \frac{p}{q}$, with q being an *odd* integer, for the FQHE.

In an ideal (non-interacting and disorder free) two-dimensional (2D) electron gas, an external magnetic field applied perpendicular to the electron plane influences the orbital motion of the electron and the energy spectrum is quantized into highly degenerate *Landau levels* with energies

$$\mathcal{E} = \left(n + \frac{1}{2} \right) \hbar \omega_c,$$

where $\omega_c = eB/m^*$ is the cyclotron energy (~ 10 meV for a magnetic field of $B = 10$ Tesla). The number of states per unit area is $N_\Phi = eB/h = 1/2\pi \ell_0^2$, where $\ell_0 = (\hbar/eB)^{\frac{1}{2}}$ is the magnetic length. In units of the flux quantum, $\Phi_0 = h/e$, $N_\Phi = B/\Phi_0$. Therefore in an area $\mathcal{A}$, $N_\Phi = \Phi/\Phi_0$, the number of flux quanta threading through that area, which is the Landau level degeneracy in area $\mathcal{A}$. The Landau level filling factor is then

$$\nu = N_e/N_\Phi = 2\pi \ell_0^2 n_e,$$

where N_e is the number of electrons and n_e is the electron density in the system.

For an integer filling factor, $\nu = j$, the lowest j Landau levels are completely filled. The next electron that is added to the system must then go to the next energy level which requires a jump across the energy gap $\hbar \omega_c$. At very low temperatures where the thermal energy is much lower than the cyclotron energy, the presence of a gap guarantees a dissipationless flow of current as indicated by the vanishing longitudinal conductivity. The FQHE occurs when the magnetic field is so strong that electrons partially fill only the lowest Landau level (LLL). In this case, for noninteracting electrons the ground state is macroscopically degenerate. It is the Coulomb interaction between the electrons that lifts the degeneracy and opens a gap [8, 71]. The origin of the FQHE cannot therefore be understood based on the behavior of

individual electrons in a magnetic field. It is the behavior of the collective ensemble wherein lies the clue, i.e., in the language of Laughlin [6, 9], it is an *emergent* phenomenon. In the words of Störmer, electrons in this state conduct "*an elaborate, mutual, quantum-mechanical dance*" [4]. The nature of that state is discussed below.

8.1.1 A Novel Many-Body Incompressible State

The problem we face in describing the origin of the FQHE[1] can be clearly stated. We have at our disposal, N_e two-dimensional electrons moving on a plane perpendicular to a magnetic field B. The field is so strong that the energy separation between adjacent Landau levels and the spin Zeeman energy are far greater than the characteristic energy scale of the electron-electron (Coulomb) interactions. Mixing of Landau levels can then be safely neglected. In that case, our job at hand is to evaluate the energy spectrum and the wave functions of the system in the lowest Landau level. We also need to determine the nature and origin of the excitation gap. It is seemingly an intractable many-body problem with no small parameter present.

In 1983, just a year after the report of the discovery of the FQHE, Laughlin proposed, based on an inspired guess, the celebrated trial wave function for the many-electron state in the LLL [5]

$$\Psi_q(z_1 \cdots z_{N_e}) = \prod_{i<j}(z_i - z_j)^q \exp\left(-\sum_i |z_i|^2/4\right) \tag{8.1}$$

where $z \equiv x + iy$ is the (complex) electron position and q is an odd integer thus satisfying the antisymmetry requirement. By counting the maximal power of each z_i one can easily verify that the wave function given above corresponds to $\nu = \frac{1}{q}$ when $N_e \to \infty$ [71]. An important property of this wave function is that, it vanishes as the q-th power when one electron approaches the other [71]. This property minimizes the Coulomb interaction energy and hence the ground state energy. The wave function describes a uniform density charge-neutral liquid state in which the electrons condense [71].

Laughlin then explained why the $\nu = \frac{1}{3}$ state is so special. The many-electron system at this filling factor is in fact, *incompressible*, and there exists an energy gap. The energy gap implies that there is a positive discontinuity in the chemical potential at this filling factor [11], which means a vanishing compressibility. The chemical potential jump has indeed been measured experimentally for the FQHE states [12]. Starting with the $\nu = \frac{1}{q}$ state if we increase or decrease the number of states by one, elementary excitations containing *fractional charge*, $e^* = \mp\frac{e}{q}$ are created [71]. These 'quasiparticles' also obey fractional statistics [13].

---

[1]In this brief introduction to the FQHE, we limit ourselves only to the description of the filling factor $\nu = \frac{1}{q}$. Interested readers could consult other sources for a more detailed account [8, 10, 71].

Laughlin's theory for the FQHE is like good poetry in physics, rich in profound ideas that has inspired researchers for decades and even from many other subfields of physics [14]. Its novel concepts on correlated quantum fluids were certainly unconventional in the field where it was applied, viz. the semiconductors. In explaining a truly remarkable macroscopic quantum phenomenon, Lauglin opened a floodgate of novel ideas with a flow that is yet to subside. Description of all those ideas is however, far beyond the scope of this brief introduction.

8.1.2 Pseudopotential Description of Interacting Electrons

In the FQHE regime where the magnetic field is so strong that the spacing between the Landau levels are (in the absence of any disorder) much larger than e.g., the thermal energy, and all the degree of freedom are confined to a single Landau level. In that situation, the Hamiltonian of the system is simply the projected interparticle interaction. Haldane was the first to point out [15] that the interaction energy of a pair of particles with the same Landau indices can be written as

$$\mathcal{H}_{ij} = \sum_{m=0}^{\infty} V_m \mathcal{P}_{ij}^m,$$

where $\mathcal{P}_{ij}^m$ projects the pair of particles i, j onto the relative angular momentum m. Antisymmetry of the electron wave function dictates that m is an odd integer. The parameters V_m are the so-called Haldane pseudopotentials, which are defined as the energy of two electrons with the relative angular momentum m. They are determined by the structure of the wave functions of the corresponding Landau level and for the n-th Landau level can be found from the following expression [15]

$$V_m^{(n)} = \int_0^\infty \frac{dq}{2\pi} q V(q) \left[F_n(q) \right]^2 L_m(q^2) e^{-q^2}, \qquad (8.2)$$

where $L_m(x)$ are the Laguerre polynomials, $V(q) = 2\pi e^2/(\kappa q \ell_0)$ is the Coulomb interaction in the momentum space, κ is the background dielectric constant, and $F_n(q)$ is the form factor of the n-th Landau level. The form factor is completely determined by the n-th Landau level wave functions. For conventional semiconductor systems, the form factors have the following form

$$F_n(q) = L_n(q^2/2). \qquad (8.3)$$

Therefore, any translationally and rotationally invariant two-body interaction, projected to a single Landau level can be described completely by a set of pseudopotentials.

For the repulsive Coulomb potential, the pseudopotentials decrease with increasing value of m [15]. In this context, it is interesting to note that the Laughlin state at $\nu = \frac{1}{q}$, with q being an odd integer, is quite unique. It has the property

$$\mathcal{P}_{ij}^m \Psi_L = 0, \quad \text{for } m < q.$$

The $\nu = \frac{1}{q}$ Laughlin state is a zero-energy eigenstate with only $V_m (m < q)$ being non-zero. As the mean squared distance between the electrons is proportional to q [71], the model potential is of short range. However, Haldane pointed out [16] that, when one varies the pseudopotentials between a hard-core model with only non-zero V_1 and the true Coulomb system, the overlap between the true ground state (in finite-size systems) and the Laughlin state is extremely good. This explains why the Laughlin state captures the essential physics of the FQHE state by being close to the exact ground state. It was also noted by Haldane that the pair interaction potential $\mathcal{H}_{ij}$ after projection into the subspace of fixed Landau index is discrete [15]. This is the central feature of the physics underlying the incompressible many-electron states that gives rise to the FQHE [8, 15].

8.1.3 Composite Fermions and the Fermion-Chern-Simons Theory

In addition to the primary filling factors, $\nu = \frac{1}{q}$ (with q as an odd integer), which correspond to the Laughlin states, the FQHE was also observed in many other higher-order fractional fillings of the Landau levels, such as $\nu = \frac{2}{5}, \frac{3}{7}, \frac{4}{9}$, and so on [3, 71]. Some of those filling factors, such as $\nu = \frac{2}{3}$, can be explained by the particle-hole symmetry [71], while the presence of other filling factors can be described within the composite fermion approach [17–19] and the Chern-Simons theory [20, 21]. The hierarchy of the FQHE states based on the composite fermion picture is constructed in the following way [17–19]. If the many-electron system is placed in a magnetic field B^* such that the filling factor of the system is $\nu^* = n_0 \Phi_0 / B^*$, where n_0 is the electron density, then by multiplying the corresponding multi-particle wave function, Ψ^* by a symmetric factor

$$F_p(z_1, \ldots, z_N) = \prod_{j < k} (z_j - z_k)^{2p} \tag{8.4}$$

where p is a positive integer, we construct the wave function, $\Psi = F_p \Psi^*$ corresponding to a new filling factor ν. To find the relation between ν^* and ν we notice that the factor F_p introduces an additional effective magnetic field, $\Delta B = 2p n_0 \Phi_0$ in the system. In fact, if we consider a particle travelling in a large orbit covering an area $\mathcal{A}$ and encloses $n_0 \mathcal{A}$ other particles, then due to the additional factor F_p that particle acquires an extra phase factor $2p 2\pi n_0 \mathcal{A} = 2\pi (\Delta B \mathcal{A} / \Phi_0)$. Therefore, the additional factor, F_p in the many-particle wave function can be thought of as an extra magnetic field, ΔB. Then the relation between the magnetic field B^*, corresponding to the filling factor ν^* and the new magnetic field B becomes

$$B = B^* + \Delta B = B^* + 2p n_0 \Phi_0 = B^* (1 + 2p \nu^*). \tag{8.5}$$

Therefore, the filling factor corresponding to the wave function Ψ, i.e., for n_0 particles in a magnetic field B, is

$$\nu = \frac{\nu^*}{2p\nu^* + 1}. \tag{8.6}$$

Multiplying the many-particle wave function by the complex conjugated factor F_p^*, we can construct the wave function corresponding to the filling factor $\frac{\nu^*}{2p\nu^*-1}$. The factor F_p thus introduces $2p$ magnetic flux quanta attached to each electron, thereby creating a composite fermion. On average, such magnetic fluxes produce an effective magnetic field, ΔB. If we start with completely filled Landau levels with integer filling factor n, then multiplication by the factor F_p, i.e., attaching the magnetic flux quanta to the electrons produces the fractional filling factors of the form

$$\nu = \frac{n}{2pn \pm 1}. \tag{8.7}$$

As an example, for $n = 2$, $p = 1$ we obtain $\nu = \frac{2}{5}$. Therefore, the integer filling factor of the composite fermions, i.e., electrons with even number of flux quanta, corresponds to fractional filling factor of real electrons. Since the ground state of the composite fermion system is incompressible, we can assume that the ground state of actual electrons with fractional filling is also incompressible. Numerical comparison of composite fermion wave functions and the exact wave functions evaluated in finite-size systems shows that the composite fermion approach indeed provides a good description of the FQHE ground states at general filling factors. The composite fermion description of FQHE states is closely related to the Chern-Simons theory of the quantum Hall systems [20, 21]. Within the Chern-Simons theory, a gauge Chern-Simons magnetic field is introduced through an unitary transformation. Such a gauge field introduces an even number of magnetic flux quanta attached to the electrons. Within the mean-field approximation, the Chern-Simons magnetic field is replaced by an uniform average magnetic field, which reproduces the same effective filling factors as in the composite fermion approach. In the Chern-Simons approach, one can go beyond the mean-field approximation and calculate low-energy excitation properties of the quantum systems. One of the applications of the Chern-Simons theory is the description of the $\nu = \frac{1}{2}$ quantum state. In this case an external magnetic field exactly cancels the mean Chern-Simons field and the composite fermions experience no average magnetic field. Therefore the $\nu = 1/2$ quantum system in this picture is equivalent to an electron system in the absence of an external magnetic field. Experimental indications of such a situation, e.g., the existence of a Fermi surface [22] at this filling factor provides ample support for this theoretical picture.

8.2 The Advent of Graphene

Just when everyone thought the glory days of the QHEs are perhaps over, along came graphene [23–25]. It is a single sheet of carbon atoms arranged in a honeycomb (hexagonal) lattice, often described as a molecular chicken wire where one carbon atom sits at each 120° corner. This material is perhaps the most interesting two-dimensional system possible, with unique electronic properties that are entirely different (and unexpected) from those of conventional two-dimensional systems [26]. The electronic band structure of graphene was theoretically studied as far

Fig. 8.2 The honeycomb lattice structure of graphene with two sublattices A and B. Within the nearest neighbor tight-binding approximation the atoms of sublattice A are coupled to atoms of sublattice B through the hopping integral γ_0
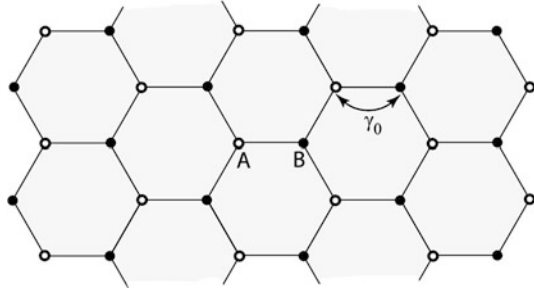
back as 1947 [27]. Electrons and holes in graphene are described as 'massless Dirac fermions' because of their linear energy dispersion near the Fermi surface [28]. Graphene is a bipartite lattice made up of two interpenetrating triangular sublattices that provides a new degree of freedom for the electronic state, the pseudospin. Transport properties of graphene exhibit many novel features, most notably (in our context), the room temperature QHE [29]. Bilayer graphene has also proven to be rich with unique properties, e.g., the gate tunable band gap. Here the energy dispersion corresponds to that of massive chiral fermions. A detailed account of all these can be found in a review article by the present authors [30].

Since its isolation in 2004 [25], graphene has maintained a dominant presence in the community. By August 2011, there were more than 11,000 publications with the word 'graphene' in their titles. With the continued plethora of articles, most notably, the superabundance of review articles [25, 28, 30–48] about various properties of graphene makes it abundantly clear that our fascination with this system is far from being over, and one expects more surprising discoveries in the coming years.

8.2.1 Massless Dirac Fermions

The two-dimensional lattice of graphene has the honeycomb structure, consisting of two inequivalent sublattices of carbon atoms, say A and B (Fig. 8.2). The nearest-neighbor tight-binding description of graphene results in a band structure with the Fermi level located at two inequivalent points, $K = (2\pi/a)(\frac{1}{3}, \frac{1}{\sqrt{3}})$ and $K' = (2\pi/a)(\frac{2}{3}, 0)$, of the first Brillouin zone. Here $a = 0.246$ nm is the lattice constant. The tight-binding approximation is valid over a wide range of energy. Within the effective mass approximation which addresses the low-energy properties, these points correspond to two valleys, K and K'. In each valley the low-energy electron dynamics near the Fermi energy is described by the following Hamiltonian [28]

$$\mathcal{H}_\xi = \xi v_F \begin{pmatrix} 0 & p_- \\ p_+ & 0 \end{pmatrix}, \tag{8.8}$$

where $p_- = p_x - ip_y$, $p_+ = p_x + ip_y$, and **p** is the two-dimensional momentum of an electron. Here $v_F \approx 10^6$ m/s is the Fermi velocity, which can be related to

the hopping integral, γ_0, between the nearest neighbor sites, $v_F = \sqrt{3}\gamma_0 a/2\hbar$. The index ξ is 1 and -1 for valleys K and K$'$, respectively. Without the spin-orbit interaction [49–51], each level determined by the Hamiltonian (8.8) has a two-fold spin degeneracy. The wave functions corresponding to the Hamiltonian (8.8) have two components belonging to sublattices A and B, and can be expressed as $(\psi_A, \psi_B)^T$ for valley K and $(\psi_B, \psi_A)^T$ for valley K$'$, where ψ_A and ψ_B are wave functions of sublattices A and B, respectively. The superscript T indicates the transpose of a vector.

The single-electron states obtained from the Hamiltonian (8.8) has a linear dispersion relation given by

$$\varepsilon(p) = \pm v_F p, \tag{8.9}$$

which is the dispersion relation of Dirac "relativistic" massless particles. In addition to spin degeneracy, each energy level has a two-fold valley degeneracy. The smooth impurity potentials or electron-electron interactions introduce coupling of different valleys. However, due to the large momentum separation of the valley states this coupling is weak and can be safely ignored.

8.2.2 Landau Levels in Graphene

In the tight-binding model the magnetic field is introduced through the Peierls substitution which introduces a magnetic field dependence of the hopping integrals. Within this approach the Landau levels with low, intermediate and very high indices can be obtained. Formation of the incompressible liquids in graphene due to electron-electron interactions is expected to occur at low Landau level indices. To study those Landau levels the effective mass approximation described by the Hamiltonian (8.8) is fully adequate. The magnetic field is introduced in the Hamiltonian (8.8) by replacing the electron momentum $\mathbf{p}$ with the generalized momentum $\boldsymbol{\pi} = \mathbf{p} + e\mathbf{A}/c$ where $\mathbf{A}$ is the vector potential. Then the Hamiltonian of an electron in a perpendicular magnetic field in valley ξ takes the form

$$\mathcal{H}_\xi = \xi v_F \begin{pmatrix} 0 & \pi_- \\ \pi_+ & 0 \end{pmatrix}. \tag{8.10}$$

The eigenfunctions of the Hamiltonian (8.10) can be expressed in terms of the conventional Landau wave functions, $\phi_{n,m}$ [52], for a particle obeying the parabolic dispersion relation with the Landau index n and intra-Landau index m, which depends on the choice of the gauge. For example, in the Landau gauge, $A_x = 0$ and $A_y = Bx$, the index m is the y-component of the momentum, while in the symmetric gauge, $\mathbf{A} = \frac{1}{2}\mathbf{B} \times \mathbf{r}$, the index m is the z-component of electron angular momentum. For these wave functions, $\phi_{n,m}$, the operators π_+ and π_- are the raising and lowering operators, respectively. This means that they increase or decrease the Landau level index, n:

$$v_F \pi_+ \phi_{n,m} = -i\hbar\omega_B \sqrt{n+1}\phi_{n+1,m},$$

$$v_F \pi_- \phi_{n,m} = i\hbar\omega_B \sqrt{n}\phi_{n-1,m},$$

where $\omega_B = \sqrt{2}v_F/\ell_0$, and ℓ_0 is the magnetic length defined in Sect. 1. The Landau eigenfunctions of the Hamiltonian (8.10) can then be written in the form

$$\Psi_{n,m} = \begin{pmatrix} i^{n-1}\chi_1\phi_{n-1,m} \\ i^n \chi_2\phi_{n,m} \end{pmatrix}, \tag{8.11}$$

where the coefficients χ_1 and χ_2 satisfy the following eigenvalue matrix equations

$$\varepsilon\chi_1 = -\xi\hbar\omega_B\chi_2 \tag{8.12}$$

$$\varepsilon\chi_2 = -\xi\hbar\omega_B\chi_1. \tag{8.13}$$

The resulting discrete Landau energy spectrum has both negative (valence band) and positive (conduction band) values, which are described by introducing integer values for the Landau index $n = 0, \pm 1, \pm 2, \ldots$, which also include the negative values of n. In terms of n, the Landau energy spectrum of electrons in graphene takes the form

$$\varepsilon_n = \hbar\omega_B \, \mathrm{sgn}(n)\sqrt{|n|}, \tag{8.14}$$

where

$$\mathrm{sgn}(n) = \begin{cases} 0 & (n=0) \\ 1 & (n>0) \\ -1 & (n<0). \end{cases} \tag{8.15}$$

Each energy level (8.14) has a two-fold valley degeneracy. The wave functions corresponding to the Landau levels (8.14) can be obtained from (8.12)–(8.13) in the following form

$$\Psi_{n,m}^K = \begin{pmatrix} \psi_A \\ \psi_B \end{pmatrix} = C_n \begin{pmatrix} \mathrm{sgn}(n)i^{|n|-1}\phi_{|n|-1,m} \\ i^{|n|}\phi_{|n|,m} \end{pmatrix}, \tag{8.16}$$

for valley K ($\xi = 1$) and

$$\Psi_{n,m}^{K'} = \begin{pmatrix} \psi_B \\ \psi_A \end{pmatrix} = C_n \begin{pmatrix} \mathrm{sgn}(n)i^{|n|-1}\phi_{|n|-1,m} \\ i^{|n|}\phi_{|n|,m} \end{pmatrix}, \tag{8.17}$$

for valley K' ($\xi = -1$). Here $C_n = 1$ for $n = 0$ and $C_n = 1/\sqrt{2}$ for $n \neq 0$.

The Landau levels in graphene have a square-root dependence on both the magnetic field and the Landau level index. For $v_F \sim 10^6$ m/s, the Landau level energy spectrum takes the form, $\varepsilon_n \approx 36\sqrt{B[\text{Tesla}]}\sqrt{n}$ (meV). This behavior is clearly different from that in conventional (henceforth called *non-relativistic* to distinguish it from the graphene system) semiconductor 2D system with a parabolic dispersion relation, for which the energy spectrum has a linear dependence on both the magnetic field and the Landau level index. As an example, for the GaAs system the Landau energy spectrum is $\varepsilon_n^{\text{GaAs}} = \hbar\omega_c(n + \frac{1}{2}) \approx 1.7B[\text{Tesla}](n + \frac{1}{2})$ (meV). The Landau level spectra for graphene and for the GaAs systems are shown in Fig. 8.3, which illustrates their different behaviors.

Fig. 8.3 The Landau levels
as a function of the
perpendicular magnetic field
for graphene (*red solid lines*)
and a GaAs system (*black
solid lines*). Numbers next to
the lines are Landau level
indices. In the case of
graphene, only the Landau
levels with positive energy,
corresponding to the
conduction band, are shown
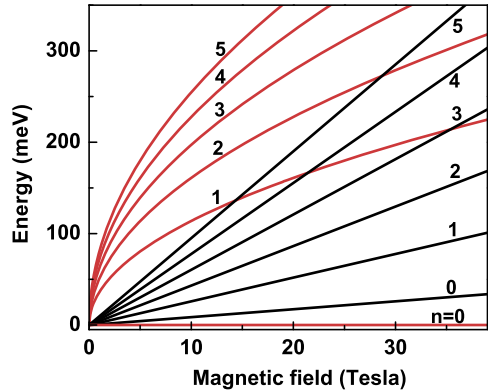
It is noteworthy that the $n = 0$ Landau level in graphene has zero energy at all
values of the magnetic field. It is populated equally by electrons and holes. The
wave functions at this Landau level are identical to those of $n = 0$ non-relativistic
Landau level [see (8.16)–(8.17)]. Therefore the interaction properties and the FQHE
of the $n = 0$ Landau level in graphene are the same as for the non-relativistic $n = 0$
Landau level. The wave functions in higher Landau levels ($|n| \geq 1$) are mixtures of
non-relativistic Landau wave functions belonging to different Landau level indices.
Therefore the interaction effects in these Landau levels should be very different
from those of the non-relativistic systems. The nature of the Landau levels, in par-
ticular the lowest level, can be effectively studied by measuring the quantum Hall
activation gaps in graphene. Measurements of the inter-Landau level activation gap
in graphene [53] revealed that the lowest LL is very sharp in contrast to the broad-
ened higher LLs, and the measured gap between the zeroth and the first Landau level
approaches the bare Landau-level splitting for high magnetic fields.
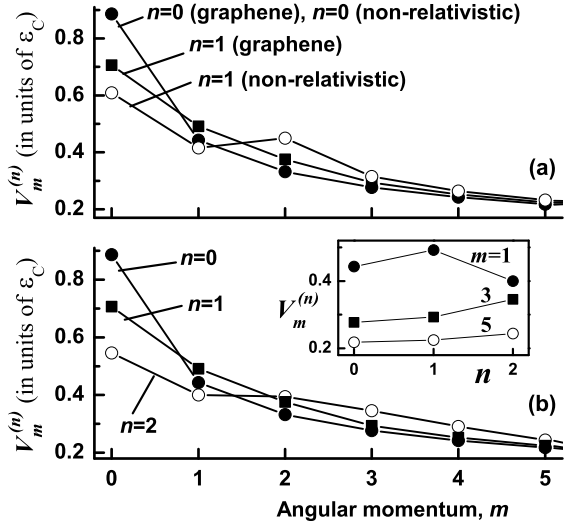
8.2.3 Pseudopotentials in Graphene

As mentioned earlier, the interaction properties of electrons within a single Lan-
dau level are completely determined by the Haldane pseudopotentials (8.2). With
the known wave functions (8.16)–(8.17), the form factors in (8.2), can be readily
evaluated. For the n-th graphene Landau level,[2] they are given by the following
expressions [see (8.3)] [55, 72]

$$F_0(q) = L_0(q^2/2) \tag{8.18}$$

$$F_n(q) = \frac{1}{2}\big[L_n(q^2/2) + L_{n-1}(q^2/2)\big]. \tag{8.19}$$

---

[2]If not otherwise stated, in what follows, we consider the positive values of n.

Fig. 8.4 The Haldane pseudopotentials shown as a function of the relative angular momentum for non-relativistic and graphene systems at $n = 0, 1$ Landau levels (**a**) and for graphene at $n = 0, 1$ and 2 Landau levels (**b**). The *inset* in panel (**b**) shows the dependence of the pseudopotentials on the Landau level index n for graphene. The energy is evaluated in units of ε_C

With these form factors the pseudopotentials for graphene are then calculated from (8.2). The pseudopotentials are given in units of the Coulomb energy, $\varepsilon_C = e^2/\kappa \ell_0$, where κ is the background dielectric constant of the system.

To compare the interaction properties of graphene and the conventional non-relativistic systems, we present in Fig. 8.4 the pseudopotentials calculated from (8.2) for graphene and for the non-relativistic system. Since the FQHE can be realized only in the low-index Landau levels, in Fig. 8.4 the results are shown only for small values of n ($n \leq 2$). As it was mentioned above, for $n = 0$ graphene and a non-relativistic system have the same pseudopotentials [Fig. 8.4(a)]. In a higher Landau level index there is an important difference in the behavior of the pseudopotentials in these two systems. More specifically, for $n = 1$, the graphene system shows a stronger electron-electron repulsion, i.e., a larger pseudopotential, at small relative angular momentum, $m < 2$, and a weaker repulsion at a large angular momentum, $m \geq 2$, compared to that for a non-relativistic system [Fig. 8.4(a)]. Based on the general properties of the Laughlin incompressible state, we can conclude that the stronger repulsion at small values of the angular momentum implies a more stable FQHE state.

In Fig. 8.4(b), the pseudopotentials of graphene are shown for different Landau levels. Due to the antisymmetry of the electronic wave functions, only the pseudopotentials with odd relative angular momenta contribute to the spin-polarized FQHE states. Hence only the pseudopotentials with $m = 1, 3, 5, \ldots$ determine the spin-polarized, and in the case of graphene, the valley-polarized properties of the system. For these values of m the pseudopotentials in the $n = 1$ Landau level show an interesting behavior: while for $m = 3$ and 5 the pseudopotential, $V_m^{(n)}$, monotonically increases with n, and for $m = 1$, the pseudopotential $V_1^{(n)}$ has a maximum at $n = 1$ [see inset in Fig. 8.4(b)]. Therefore the electrons with relative angular momentum $m = 1$ show the strongest repulsion in the $n = 1$ Landau level. This is different from

Table 8.1 Characteristics of Haldane pseudopotentials for graphene and for conventional electron systems

	$V_1^{(n)}/V_3^{(n)}$	$V_3^{(n)}/V_5^{(n)}$
$n = 0$ (graphene)	1.60	1.26
$n = 0$ (non-relativistic)	1.60	1.26
$n = 1$ (graphene)	1.68	1.33
$n = 1$ (non-relativistic)	1.32	1.36

the behavior of a non-relativistic system, where the strongest repulsion is in the lowest $n = 0$ Landau level.

The stability of the incompressible FQHE state, i.e., the magnitude of the FQHE gap, depends on how fast the pseudopotentials decay with increasing relative angular momentum. For spin and valley polarized electron systems this decay is determined by the ratios $V_1^{(n)}/V_3^{(n)}$ and $V_3^{(n)}/V_5^{(n)}$. The larger the ratios, the more stable is the FQHE. In Table 8.1, the values of the ratios are shown for graphene and for non-relativistic systems in the two lowest Landau levels with $n = 0$ and 1. These values clearly indicate that $V_1^{(n)}/V_3^{(n)}$ has the largest value for graphene in the $n = 1$ Landau level which suggests that the gaps of the FQHE states should have the largest value in graphene in the $n = 1$ Landau level.

8.2.4 Nature of the Incompressible States in Graphene

Each Landau level in graphene is four-fold degenerate due to two-fold valley and two-fold spin degeneracies. The spin degeneracy is partially lifted due to the Zeeman splitting, which is $\Delta_Z = g\mu_B B \approx 1.5B$ [Tesla] (K) $\approx 0.13B$ [Tesla] (meV), where $g \approx 2.2$. The symmetry-breaking terms should be compared with the typical energy of the inter-electron interactions within a single Landau level, which is the Coulomb energy, $\varepsilon_C = e^2/\kappa\ell_0$. The Coulomb energy determines the magnitude of the Haldane pseudopotentials and in graphene it is $\varepsilon_C \approx (54/\kappa)\sqrt{B\,[\text{Tesla}]}$ (meV). For $\kappa \approx 4$ the Coulomb energy becomes $\varepsilon_C \approx 14\sqrt{B\,[\text{Tesla}]}$ (meV). Due to the small value of the dielectric constant, the Coulomb energy in graphene is a few times larger than the corresponding energy in a non-relativistic system, where the dielectric constant is about $\kappa \sim 13$. Although the Coulomb interaction in graphene is strong, it is still less than the inter-Landau level spacing. For example, the energy separation between the $n = 0$ and $n = 1$ Landau levels in graphene is $36\sqrt{B[\text{Tesla}]}$ (meV) (see Sect. 8.2.2). The Coulomb interaction also introduces the valley-symmetry breaking terms [55, 56], which are algebraically small in a/ℓ_0. For typical values of the magnetic field, the Zeeman energy in graphene is almost two orders of magnitude smaller than the Coulomb energy, $\Delta_Z/\varepsilon_C \approx 0.01\sqrt{B\,[\text{Tesla}]}$, and within a good approximation, a single Landau level in graphene can be considered as the four-fold degenerate level. Electrons within a single Landau level therefore have the SU(4) symmetry with weak symmetry breaking terms due to the Zeeman splitting and the valley asymmetry terms in the interaction Hamiltonian.
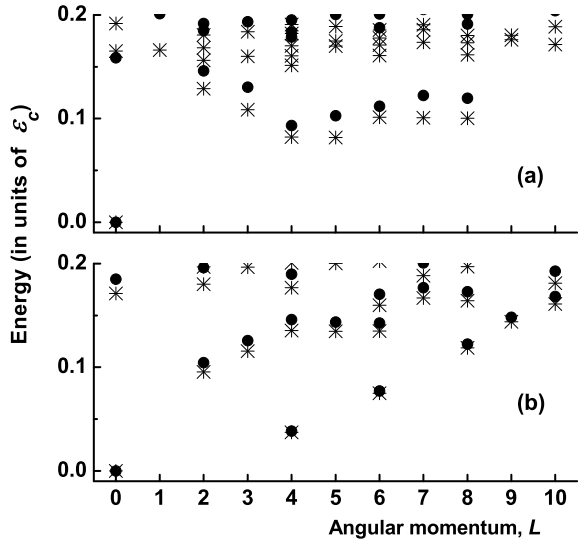
The properties of the FQHE are determined by the nature of the ground states, e.g., valley or spin polarization of the ground states, and the value of the FQHE gap, which characterizes the stability of the FQHE with respect to the temperature and the disorder. Theoretically, the FQHE states are generally studied by numerical diagonalization of the Hamiltonian matrix for finite-size electron systems in either the planar (torus) or the spherical geometry [71]. In the spherical geometry [16, 57–59] the magnetic field is introduced in terms of the integer number $2S$ of magnetic flux quanta through the sphere in units of the flux quantum. Then the radius of the sphere R is defined as $R = \sqrt{S}\ell_0$. The single-electron states are characterized by the angular momentum S, and its z component, S_z. The number of available states in a sphere is $(2S + 1)$. These states correspond to a single Landau level in the planar geometry. Then for a given number of electrons N_e the parameter S determines the filling factor of the Landau level. In the thermodynamic limit, the filling factor is $\nu = N_e/(2S + 1)$, but the exact relation between the FQHE filling factor and the number of electrons depends on the type of the FQHE state. In the spherical geometry, the many-particle states are described by the total angular momentum L and its z component, while the energy depends only on L. For the many-electron system only the lowest eigenvalues and eigenvectors of the interaction Hamiltonian matrix are calculated [58]. These eigenstates determine the nature of the ground state of the system and its neutral collective excitation gap. By varying the magnetic field flux through the system the charged excitations can be also studied.

The valley and spin polarizations of the ground states at the major FQHE filling factors, $\frac{1}{3}$, $\frac{2}{3}$, and $\frac{2}{5}$, were studied numerically for $n = 0$ and $n = 1$ Landau levels [62, 73, 75]. It was found that in the $n = 0$ Landau level the $\nu = \frac{1}{3}$ ground state is valley and spin polarized, but the $\nu = \frac{2}{3}$ and $\nu = \frac{2}{5}$ ground states are valley unpolarized [56, 73, 75]. This behavior is similar to the non-relativistic 2D system with zero Zeeman splitting, i.e., with the SU(2) symmetry. For the $n = 1$ level the graphene system however shows a different behavior. In this case, the ground states at $\nu = \frac{1}{3}$, $\frac{2}{3}$, and $\frac{2}{5}$ are all valley polarized [75]. It was also shown that for the graphene system in the $n = 0$ Landau level with filling factor $\nu = 2 + \frac{1}{3}$, the $\frac{1}{3}$ state is valley polarized even at a small Zeeman splitting [62].

The gaps of the FQHE states, i.e., the stability of the incompressible states, are determined by the Haldane pseudopotentials. From the general analysis of the pseudopotentials in different Landau levels we can conclude that the FQHE is more stable in the $n = 1$ Landau level in graphene. Therefore the largest FQHE gap is expected in the $n = 1$ Landau level. This property is illustrated in Fig. 8.5, where the energy spectra of the valley and spin polarized electron system at filling factors $\frac{1}{3}$ and $\frac{1}{5}$ are shown. In the spherical geometry, the filling factors $\nu = 1/q$ (q is an odd integer) are realized at $S = (q/2)(N_e - 1)$. The ground state of the $1/q$ FQHE is well described by the Laughlin function [5, 71].

The energy spectra of the $\nu = \frac{1}{3}$ FQHE system is shown in Fig. 8.5(a) for $N_e = 8$ electrons at the $n = 0$ and $n = 1$ Landau levels. The energy spectra in the $n = 0$ Landau level for graphene and the non-relativistic 2D system are exactly the same with the same value of the excitation gap. For a non-relativistic system this is the largest excitation gap of the $\nu = \frac{1}{3}$ FQHE state. That is not the case with graphene

where the FQHE gap has the largest value in the $n = 1$ Landau level [Fig. 8.5(a)].
For smaller filling factors, i.e., at $\nu = \frac{1}{5}$, the pseudopotentials with larger values of
the relative angular momentum determine the properties of the system. As a result,
the difference between the FQHE states in the $n = 0$ and $n = 1$ Landau levels be-
comes less pronounced, which is illustrated in Fig. 8.5(b) for $N_e = 6$ electrons and
at the filling factor $\nu = \frac{1}{5}$. This tendency is completely different from that of the
non-relativistic systems where the FQHE is strongly suppressed in the $n = 1$ Lan-
dau level. A similar conclusion about the unique interaction properties of the $n = 1$
Landau level in graphene was reported in Ref. [73], where the properties of the
FQHE states in graphene and GaAs systems were compared. In the $n = 0$ Landau
level the graphene system becomes similar to the GaAs system, while in the $n = 1$
Landau level, only the graphene system exhibits stable FQHE states.

The spectra shown in Fig. 8.5 correspond to the polarized neutral excitations of
the electron system and illustrate the relative strength of the electron-electron inter-
actions at different Landau levels in graphene. Due to the valley degeneracy of the
Landau levels in graphene, valley unpolarized excitations, which are of the type of
valley skyrmions, can have lower energies than those for polarized excitations. Nu-
merical analysis indicates that the lower-energy charged excitations at major filling
factors, $\nu = \frac{1}{3}$, $\frac{2}{3}$, and $\frac{2}{5}$, are unpolarized valley skyrmions [75].

For the SU(4) symmetric graphene electron system, i.e., at small Zeeman split-
ting, new types of FQHE states at filling factors $\nu = q/(2pq \pm 1)$ with $q \geq 3$ were
also proposed [63] in the $n = 0$ and $n = 1$ Landau levels. These states are expected
in graphene because of the interplay between the spin and valley degrees of freedom.

From the discussions above, it is quite clear that the electron-electron interactions
in graphene are more pronounced in the $n = 1$ Landau level, which should result in
more stable FQHE states with large excitation gaps in the $n = 1$ Landau level. This

is opposite to what we observe in a non-relativistic 2D system, where the strongest interactions are realized in the $n = 0$ Landau level.

8.2.5 Experimental Observations of the Incompressible States

As explained in earlier chapters, experimental demonstration of the quantum Hall plateaus at filling factors $\nu = 4(q + \frac{1}{2})$ [11, 12] quite convincingly confirmed the Dirac nature of electron dynamics in graphene that was purely non-interacting and devoid of any effects due to interactions among the electrons. Interestingly, any collective behavior due to electron-electron interactions, akin to the FQHE was found to be very difficult to observe. This is notwithstanding the strong unscreened Coulomb forces that were supposed to exist between the charge carriers. Taking the cue from earlier studies of the FQHE in a conventional two-dimensional electron gas (2DEG), it was clear that experimental observation of these states crucially depends on significantly high-quality samples where the Coulomb energy scale far exceeds that of the impurity-induced random potential fluctuations. Such a significant improvement in sample quality was indeed achieved in suspended graphene (SG) samples, where the substrate-induced perturbations were entirely eliminated [66, 67]. Observation of the quintessential $\frac{1}{3}$-FQHE in suspended graphene was first reported by two groups [68–70]. Observation of a few other fractions followed soon after.

It has been correctly pointed out by Skachko et al. [71] (also elaborated in the previous subsection) that the FQHE in graphene can be expected to deviate from that in conventional 2DEG in several important ways. First of all, electrons in graphene are dynamically more two dimensional than in semiconductor quantum wells, where the well widths range from 10–30 nm. This implies that the interaction at short distances in graphene is much stronger than in conventional quantum wells. Secondly, electron-electron interactions in SG are enhanced even further due to the absence of substrate screening ($\kappa \sim 1$) as compared to, e.g., in GaAs, where $\kappa \sim 13$. This enhanced interaction in graphene leads to a larger gap [72], and therefore the FQHE state persists at much higher temperatures. Finally, due to the four-fold spin and valley degeneracy, the situation in graphene resembles more like what would be realized in a double quantum well system, rather than a single quantum well. However, unlike in a GaAs system, the intra- and inter-well interactions in graphene are almost identical. This suggests the existence of new FQHE states which are absent in conventional systems [72, 73].

Experimental results of Andrei et al. [68, 69, 71] for quantum Hall plateaus at $\nu = \frac{1}{3}$ in monolayer SG are shown in Fig. 8.6(a) for various values of the applied magnetic field. These authors noted that the plateau at the $\frac{1}{3}$ filling factor was very robust—it appeared at ~ 2 Tesla at low temperatures (~ 1 K) and persisted up to 20 K at $B = 12$ Tesla. The robustness of the FQHE states can be further assessed by studying the excitation gap [71]. The temperature dependence of the diagonal resistivity ρ_{xx} (or diagonal conductivity σ_{xx}, since $\sigma_{xx} \sim \rho_{xx}/\rho_{xy}^2$ near the ρ_{xx} minima) is interpreted as the activation energies in the FQHE [73–75]. These energies are
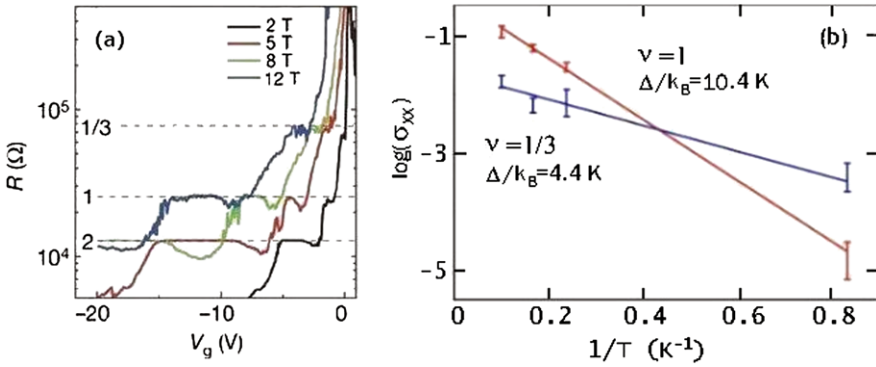
Fig. 8.6 The results of Andrei et al. [68, 69, 71]: (**a**) Gate voltage dependence of resistance for a suspended graphene sample shown at different magnetic fields and at temperature 1.2 K. The plateaus at $\nu = 1$, 2, and $\frac{1}{3}$ are clearly visible. (**b**) The activation gap at $\nu = 1$ and $\nu = \frac{1}{3}$, obtained from the temperature dependence of the diagonal conductivity
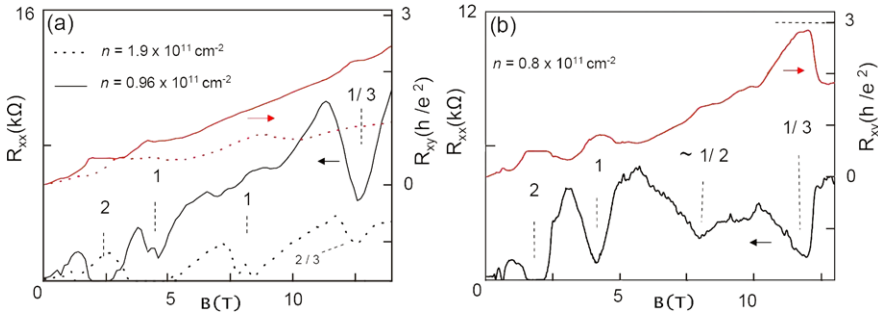

Fig. 8.7 Results of Kim et al. [70, 77]: The Hall resistance and the diagonal resistance as a function of the magnetic field for two samples in four-terminal measurements

attributed to the energy gaps of the incompressible state at $\nu = \frac{1}{3}$ that separate the many-body ground state from the excited states. Measurements of activation gaps at integer filling factors have been already reported for monolayer [53] and bilayer [76] graphene.

The activation gap at $\nu = \frac{1}{3}$ in monolayer SG, as reported by Andrei et al. [69], is shown in Fig. 8.6(b). They obtained a value of $\Delta / k_B = 4.4$ K at 12 Tesla, where k_B is the Boltzmann constant. The corresponding value at $\nu = 1$ was $\Delta / k_B = 10.4$ K. These values are much higher than those in conventional semiconductor structures. For example, in high mobility GaAs heterostructures, the $\nu = \frac{1}{3}$ activation gap is ~ 2 K at 12 Tesla. The larger gap clearly signifies the robust nature of the $\frac{1}{3}$-FQHE state in graphene.

The fractional QHE on ultraclean suspended graphene devices was also reported by Kim et al. in two-terminal [70], and in multi-terminal [77] magnetotransport measurements (Fig. 8.7). They also observed a remarkable stability of the corre-

lated state in graphene, as compared to that in a conventional 2DEG, due to the enhanced electron-electron interaction. The energy gap was measured via thermal activation, and they reported the gap to be ~ 20 K at 14 Tesla. The hierarchy of FQHE states observed experimentally [78] in high-mobility graphene samples at $n = 0$ Landau level confirms the existence of strong inter-electron interaction in graphene. For $n = 0$, this interaction results in a spontaneous breaking of the SU(4) symmetry (two spin and two valley degrees of freedom) at the FQHE filling factors. The results in Ref. [78] also suggest a strong interaction between the composite fermions within the composite fermion description of the FQHE. Therefore in the composite fermion description of the FQHE in graphene the interaction between the composite fermions should be taken into account. The large $\nu = \frac{1}{3}$-FQHE gap in the $n = 1$ Landau level observed in Ref. [78] supports the theoretical conclusion about strong electron-electron interaction in the $n = 1$ Landau level in graphene. Details about the measurements by these leading experimental groups can also be found elsewhere in this book. Finally, magnetotransport measurements on suspended bilayer and trilayer graphene systems have also been reported [79]. In bilayer systems, a small plateau at $\nu = \frac{1}{3}$ was observed. The $\frac{1}{3}$-FQH state was not observed in trilayer graphene. More experiments on bilayer graphene would certainly help resolving many of the novel effects found theoretically and discussed below.

8.3 Bilayer Graphene

Bilayer graphene consists of two coupled monolayers of graphene [80]. Depending on the orientation of the monolayers, there are two main stacking arrangements of graphene bilayer: (i) AA stacking and (ii) Bernal (AB) stacking. These two possibilities are shown schematically in Fig. 8.8. Only the nearest neighbor inter-layer coupling, characterized by the inter-layer hopping integral, γ_1, is introduced. A typical value of inter-layer hopping integral is $\gamma_1 \approx 400$ meV. Unlike in monolayer graphene, the low energy excitations in bilayer graphene are massive with a parabolic dispersion. The band structure is gapless. The dispersion can be probed by measuring the activation gaps between the neighboring Landau levels [76].

The Hamiltonian of a bilayer graphene in a perpendicular magnetic field is described by a 4×4 matrix, which, within the basis of Hamiltonian (8.10) can be expressed as

$$\mathcal{H}_\xi^{(AA)} = \xi \begin{pmatrix} 0 & v_F\pi_- & \xi\gamma_1 & 0 \\ v_F\pi_+ & 0 & 0 & \xi\gamma_1 \\ \xi\gamma_1 & 0 & 0 & v_F\pi_- \\ 0 & \xi\gamma_1 & v_F\pi_+ & 0 \end{pmatrix}, \tag{8.20}$$

for the AA stacking and

$$\mathcal{H}_\xi^{(AB)} = \xi \begin{pmatrix} 0 & v_F\pi_- & 0 & 0 \\ v_F\pi_+ & 0 & \xi\gamma_1 & 0 \\ 0 & \xi\gamma_1 & 0 & v_F\pi_- \\ 0 & 0 & v_F\pi_+ & 0 \end{pmatrix}, \tag{8.21}$$
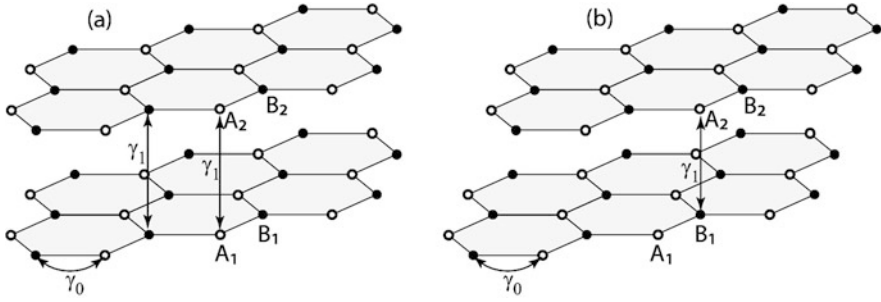
Fig. 8.8 Schematic illustration of two different stacking of bilayer graphene, consisting of two coupled monolayers of graphene: (**a**) AA stacking; (**b**) Bernal (AB) stacking. Each graphene layer consists of two inequivalent sites A and B. The intra-layer and intra-layer hopping integrals are shown by γ_0 and γ_1, respectively

for the Bernal stacking. The Hamiltonians (8.20)–(8.21) are expressed in the basis $(\psi_{A_1}, \psi_{B_1}, \psi_{A_2}, \psi_{B_2})^T$ for the K valley ($\xi = 1$) and $(\psi_{B_2}, \psi_{A_2}, \psi_{B_1}, \psi_{A_1})^T$ for the K′ valley ($\xi = -1$), where the superscript 'T' indicates the transpose of a vector. Here A_1, B_1 and A_2, B_2 correspond to sublattices of monolayers 1 and 2, respectively.

8.3.1 Magnetic Field Effects

In an external magnetic field each monolayer has discrete sets of Landau levels, which are coupled in bilayer graphene. For the AA and AB stackings the coupling of Landau levels have different structures. For the AA stacking the coupling occurs between the same Landau levels, i.e., with the same Landau index n, of two monolayers, resulting in a splitting of the initially degenerate Landau levels of two monolayers. The wave functions of bilayer graphene with AA stacking have the following form

$$\Psi_{n,m}^{(bi,AA)} = \begin{pmatrix} \Psi_{n,m}^{(mono)} \\ \pm\Psi_{n,m}^{(mono)} \end{pmatrix} \sim \begin{pmatrix} \phi_{|n|-1,m} \\ \phi_{|n|,m} \\ \phi_{|n|-1,m} \\ \phi_{|n|,m} \end{pmatrix}, \tag{8.22}$$

which shows that the wave functions of bilayer graphene with AA stacking are a mixture of $|n|$-th and $(|n| - 1)$-th non-relativistic Landau wave functions [81]. The Haldane pseudopotentials of bilayer Landau levels are completely identical to the corresponding pseudopotentials of the monolayer graphene. Therefore the FQHE in such a bilayer does not bring in any new features.

A different situation occurs for the Bernal stacking, which introduces coupling between different Landau levels of the two layers. The structure of the wave functions of such a bilayer graphene is as follows

$$\Psi_{n,m}^{(bi,AB)} \sim \begin{pmatrix} \phi_{|n|-1,m} \\ \phi_{|n|,m} \\ \phi_{|n|,m} \\ \phi_{|n|+1,m} \end{pmatrix}. \tag{8.23}$$

In this case the wave functions of bilayer graphene correspond to mixtures of the non-relativistic Landau wave functions with indices $n - 1$, n, and $n + 1$. Such a mixture can modify the interaction within a single Landau level of bilayer graphene and can influence the properties of the FQHE in this system. In what follows, we consider only the bilayer graphene with Bernal stacking.

8.3.2 Biased Bilayer Graphene

In addition to the inter-layer coupling, there are few other parameters, which can control the interaction properties of bilayer graphene. These parameters are inter-layer bias voltage, U, which can be varied for a given system [82, 83], and the intra-layer asymmetry, Δ, in the bottom layer, which is in contact with a substrate. Such an asymmetry depends on the substrate and results in different on-site energies for sublattices A_1 and B_1. With these additional terms the Hamiltonian of bilayer graphene with Bernal stacking (for valley $\xi = \pm 1$) takes the form [84]

$$\mathcal{H}_{\xi}^{(AB)}$$

$$= \xi \begin{pmatrix} \frac{U}{2} + \frac{\Delta}{4}(1+\xi) & v_F\pi_- & 0 & 0 \\ v_F\pi_+ & \frac{U}{2} - \frac{\Delta}{4}(1+\xi) & \xi\gamma_1 & 0 \\ 0 & \xi\gamma_1 & -\frac{U}{2} + \frac{\Delta}{4}(1-\xi) & v_F\pi_- \\ 0 & 0 & v_F\pi_+ & -\frac{U}{2} - \frac{\Delta}{4}(1-\xi) \end{pmatrix}. \tag{8.24}$$

The eigenfunctions of Hamiltonian (8.24) have the following form [see (8.23)]

$$\Psi_{n,m}^{(bi)} = \begin{pmatrix} \xi C_1\phi_{|n|-1,m} \\ i C_2\phi_{|n|,m} \\ i C_3\phi_{|n|,m} \\ \xi C_4\phi_{|n|+1,m} \end{pmatrix}, \tag{8.25}$$

where the coefficients, C_1, C_2, C_3, and C_4, can be found from the following linear system of equations

$$\varepsilon C_1 = \left[\xi u + \delta(1+\xi)\right]C_1 - \sqrt{n}C_2 \tag{8.26}$$

$$\varepsilon C_2 = \left[\xi u - \delta(1+\xi)\right]C_2 - \sqrt{n}C_1 + \tilde{\gamma}_1 C_3 \tag{8.27}$$

$$\varepsilon C_3 = \left[-\xi u - \delta(1-\xi)\right]C_3 + \sqrt{n+1}C_4 + \tilde{\gamma}_1 C_2 \tag{8.28}$$

$$\varepsilon C_4 = \left[-\xi u + \delta(1-\xi)\right]C_4 + \sqrt{n+1}C_3, \tag{8.29}$$

where all energies are expressed in units of the Coulomb energy, $\varepsilon_B = \hbar v_F / \ell_0$, ε is the energy of the Landau level, $\delta = \Delta/(4\varepsilon_B)$, $u = U/(2\varepsilon_B)$, and $\tilde{\gamma}_1 = \gamma_1/\varepsilon_B$.

Then the eigenvalue equation which determines the Landau energy spectrum of bilayer graphene is given by [85]

$$
\begin{aligned}
\big[(\varepsilon + \xi u)^2 &- \delta^2(1-\xi)^2 - 2n\big]\big[(\varepsilon - \xi u)^2 - \delta^2(1+\xi)^2 - 2(n+1)\big] \\
&= \tilde{\gamma}_1^2\big[(\varepsilon - \delta)^2 - (u+\delta)^2\big].
\end{aligned}
\tag{8.30}
$$

For each value of $n \geq 0$ there are four solutions of the eigenvalue equation (8.30), corresponding to four Landau levels in a bilayer graphene for a given valley, $\xi = \pm 1$. For convenience, let us introduce the following labelling scheme for these Landau levels. The four Landau levels correspond to two valence levels which usually have negative energies, and two conduction levels, which have positive energies. Then the four Landau levels of bilayer graphene for a given value of n ($n \geq 0$) and a given valley, ξ, can be labelled as $n_i^{(\xi)}$, where $i = -2, -1, 1, 2$ is the label of the Landau level in the ascending order of energy. Here negative and positive values of i correspond to valence and conduction levels, respectively. For zero bias voltage, $U = 0$, and zero intra-layer asymmetry, $\Delta = 0$, these four Landau levels are

$$
\varepsilon = \pm\sqrt{2n+1+\frac{\tilde{\gamma}_1^2}{2} \pm \frac{1}{2}\sqrt{\left(2+\tilde{\gamma}_1^2\right)^2 + 8n\tilde{\gamma}_1^2}}.
\tag{8.31}
$$

In this case each Landau level has two-fold valley degeneracy, i.e., no dependence on the index ξ in (8.31). For finite values of U and Δ, the valley degeneracy is lifted. For zero intra-layer asymmetry, $\Delta = 0$, the Landau energy spectra of two valleys are not independent. They are related through the equation $\varepsilon(n_i^{(\xi)}) = -\varepsilon(n_{-i}^{(-\xi)})$, where $\varepsilon(n_i^{(\xi)})$ is the energy of the Landau level $n_i^{(\xi)}$.

The coefficients C_1, C_2, C_3, and C_4, determined from the solution of the eigenvalue equation (8.30) and the system of equations (8.26)–(8.29), are expressed as

$$
C_1 = f\left[\frac{2\tilde{\gamma}_1 n}{[\varepsilon + \xi u - \delta(1-\xi)][(\varepsilon + \xi u)^2 - \delta^2(1-\xi)^2 - 2n]}\right]^{\frac{1}{2}}
$$

$$
C_2 = f\left[\frac{\tilde{\gamma}_1[\varepsilon - \xi u - \delta(1+\xi)]}{[(\varepsilon - \xi u)^2 - \delta^2(1+\xi)^2 - 2(n+1)]}\right]^{\frac{1}{2}}
$$

$$
C_3 = f\left[\frac{\tilde{\gamma}_1[\varepsilon + \xi u - \delta(1-\xi)]}{[(\varepsilon + \xi u)^2 - \delta^2(1-\xi)^2 - 2n]}\right]^{\frac{1}{2}}
$$

$$
C_4 = f\left[\frac{2\tilde{\gamma}_1(n+1)}{[\varepsilon - \xi u - \delta(1+\xi)][(\varepsilon - \xi u)^2 - \delta^2(1+\xi)^2 - 2(n+1)]}\right]^{\frac{1}{2}}.
$$

Here the constant f is determined from the normalization condition, $|C_1|^2 + |C_2|^2 + |C_3|^2 + |C_4|^2 = 1$.

Since the FQHE is expected to be observable only in the Landau levels with low values i of the index, n, we consider below the sets of Landau levels of bilayer graphene with $n = 0$ and $n = 1$ only. The wave functions of these Landau levels

are mixtures of the conventional non-relativistic Landau functions with indices 0, 1, and 2.

There are two special Landau levels of bilayer graphene which have unique properties. For $n = 0$ there is a solution of (8.30) with energy $\varepsilon = -u$ for the K valley ($\xi = 1$) and $\varepsilon = u + 2\delta$ for the K' valley ($\xi = -1$). The corresponding wave function has the form

$$\Psi_{0_1,m}^{(bi)} = \begin{pmatrix} \phi_{0,m} \\ 0 \\ 0 \\ 0 \end{pmatrix}. \tag{8.32}$$

This Landau level of bilayer graphene does not have any admixture of other Landau levels and has exactly the same properties as the 0-th conventional non-relativistic Landau level. At zero u and δ this Landau level has exactly zero energy.

For small values of u and δ there is another solution of (8.30) with $n = 0$ and almost zero energy, $\varepsilon \approx 0$. The corresponding Landau level has the following wave functions

$$\Psi_{0_{-1},m}^{(bi)} = \frac{1}{\sqrt{\tilde{\gamma}_1^2 + 2}} \begin{pmatrix} \tilde{\gamma}_1 \phi_{1,m} \\ 0 \\ \sqrt{2}\phi_{0,m} \\ 0 \end{pmatrix} = \frac{1}{\sqrt{\gamma_1^2 + 2\varepsilon_B^2}} \begin{pmatrix} \gamma_1 \phi_{1,m} \\ 0 \\ \sqrt{2}\varepsilon_B \phi_{0,m} \\ 0 \end{pmatrix}. \tag{8.33}$$

The properties of this Landau level depends on the strength of the magnetic field. In a small magnetic field, $\varepsilon_B \ll \gamma_1$, the wave function becomes $(\psi_{1,m}, 0, 0, 0)^T$ and the Landau level becomes identical to the $n = 1$ non-relativistic Landau level. For a large magnetic field $\varepsilon_B \gg \gamma_1$, the Landau level wave function becomes $(0, 0, \psi_{0,m}, 0)^T$ and the bilayer Landau level has the same properties as for the $n = 0$ non-relativistic Landau level.

8.3.3 Pseudopotentials in Bilayer Graphene

Once the wave functions (8.25) of the bilayer Landau level are evaluated, the form factor in the Haldane pseudopotentials (8.2) can be obtained from

$$F_n(q) = |C_1|^2 L_{n-1}(q^2/2) + (|C_2|^2 + |C_3|^2) L_n(q^2/2) + |C_4|^2 L_{n+1}(q^2/2). \tag{8.34}$$

In fact, the shape of the form factor tells us about the interaction effects within the bilayer Landau levels. For the Landau level 0_1, defined by (8.32), the form factor is $F_{0_1} = L_0(q^2/2)$, which is exactly the same as the form factor in (8.3) of the non-relativistic system in the $n = 0$ Landau level. Therefore the interaction effect in this Landau level is the same as in the $n = 0$ non-relativistic Landau level.

The bilayer Landau level 0_{-1}, defined by (8.33), exhibits an interesting behavior of bilayer graphene with increasing magnetic fields. The form factor corresponding to that Landau level (8.33) is given by

$$F_{0_{-1}}(q) = \left[\frac{\gamma_1^2}{\gamma_1^2 + 2\varepsilon_B^2}\right]L_1\left(q^2/2\right) + \left[\frac{2\varepsilon_B^2}{\gamma_1^2 + 2\varepsilon_B^2}\right]L_0\left(q^2/2\right). \qquad (8.35)$$

With increasing magnetic field, i.e., increasing ε_B, the bilayer Landau level 0_{-1} becomes identical to (i) the $n = 1$ non-relativistic Landau level with the form factor $L_1(q^2/2)$ for a small magnetic field, $\varepsilon_B \ll \gamma_1$; (ii) the $n = 1$ Landau level of monolayer graphene with the form factor $\frac{1}{2}[L_0(q^2/2) + L_1(q^2/2)]$ for $\varepsilon_B = \gamma_1/\sqrt{2}$; and, (iii) the $n = 0$ non-relativistic Landau level with the form factor $L_0(q^2/2)$ for a large magnetic field, $\varepsilon_B \gg \gamma_1$. For typical values of γ_1, only the first regime will be accessible experimentally. For example, for $\gamma_1 = 400$ meV the condition $\varepsilon_B = \gamma_1/\sqrt{2}$ is only achieved for a magnetic field of $B = 120$ Tesla.

8.3.4 Novel Effects from Electron-Electron Interactions

Once the pseudopotentials are known, the FQHE states in a graphene bilayer can be studied using very accurate numerical techniques. Compared to monolayer graphene, bilayer graphene has additional parameters by which we can control the electron-electron interaction strength. As we recall, in monolayer graphene the interaction strength depends only on the Landau level index. In bilayer graphene the inter-electron interaction strength depends also on the magnetic field, the bias voltage U, and the intra-layer asymmetry Δ. By varying these parameters, the stability, i.e., the excitation gap of the FQHE states can therefore be controlled [86].

Stable FQHE states in bilayer graphene are expected in the $n = 0$ and $n = 1$ bilayer Landau level sets. These sets are the mixtures of $n = 0$, $n = 1$, and $n = 2$ non-relativistic Landau level wave functions. The mixture depends on the values of the parameters of the system. With a non-zero bias voltage and intra-layer asymmetry, the valley degeneracy of the Landau levels of bilayer graphene is lifted, resulting in different properties of Landau levels for different valleys.

The stability of the FQHE state is characterized by the value of the corresponding FQHE gap. For the primary filling fractions of the FQHE, i.e., $\nu = \frac{1}{3}, \frac{1}{5}, \frac{2}{5}$ etc., the bilayer system shows a similar behavior. Therefore, in what follows, only the results for the $\nu = \frac{1}{3}$ FQHE state are shown. The general behavior of the FQHE gap for different parameters of the bilayer system is illustrated in Figs. 8.9, 8.10 and 8.11. For each value of n, $n = 0$ and $n = 1$, there are four Landau levels in each valley. Within this set of bilayer Landau levels, there is one special Landau level which has an unique property. This Landau level has the label $0_1^{(+)}$ with the wave function given by (8.32), which is just the $n = 0$ non-relativistic Landau wave function for *all parameters* of bilayer graphene. Therefore, the interaction properties within this Landau level are identical to the interaction properties of the $n = 0$ non-relativistic
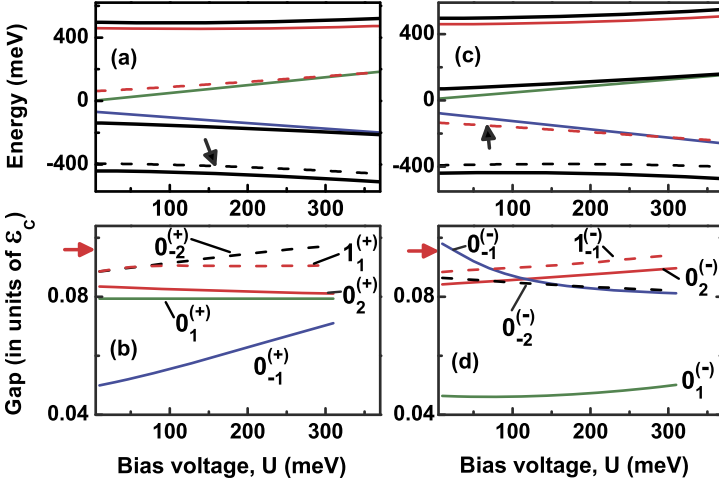
Fig. 8.9 Landau levels of bilayer graphene [panels (**a**) and (**c**)] are shown as a function of the bias voltage, U, i.e., the difference between the on-site energies in the two layers. Panels (**b**) and (**d**): the Coulomb gaps of $\frac{1}{3}$-FQHE in corresponding Landau levels. The numbers next to the lines are the labels of the Landau levels. The same types of lines [in panels (**a**) and (**b**) and panels (**c**) and (**d**)] correspond to the same Landau levels. Panels (**a**) and (**b**) correspond to valley K, while panels (**c**) and (**d**) correspond to valley K$'$. The system is characterized by $\Delta = 150$ meV, $\gamma_1 = 400$ meV, and a magnetic field $B = 15$ Tesla. The *arrows* in panels (**a**) and (**c**) show the Landau level with the strongest $\frac{1}{3}$-FQHE. The *arrows* in panels (**b**) and (**d**) indicate the gap of $\frac{1}{3}$-FQHE in the $n = 1$ Landau level of monolayer graphene

Landau level and correspondingly the $n = 0$ Landau level of monolayer graphene. The gap of the FQHE at this Landau level does not depend on the parameters of the system and is the same as that of the $n = 0$ monolayer graphene. This property is shown in Figs. 8.9–8.11 as a function of bias voltage, asymmetry parameter Δ, and the magnetic field, where it is shown that the FQHE gap of the Landau level $0_1^{(+)}$ does not depend on the parameters of bilayer graphene.

From Figs. 8.9–8.11 it is quite clear that in each valley the bilayer graphene has four Landau levels with a strong $\frac{1}{3}$-FQHE for all values of the parameters of the system. These levels have the following labels: $0_{-2}^{(+)}$, $0_1^{(+)}$, $0_2^{(+)}$, $1_1^{(+)}$ (valley K) and $0_{-2}^{(-)}$, $0_{-1}^{(-)}$, $0_2^{(-)}$, $1_{-1}^{(-)}$ (valley K$'$). Therefore for a given valley there are three Landau levels with $n = 0$ and one Landau level with $n = 1$, which all show a stable FQHE. The gaps of the corresponding FQHE states are usually between the gaps of $n = 0$ and $n = 1$ $\nu = \frac{1}{3}$-FQHE state in monolayer graphene. The value of the gap of the $\frac{1}{3}$-FQHE state in the $n = 1$ Landau level of monolayer graphene is shown by red arrows in Figs. 8.9–8.11. In the Landau level $0_{-2}^{(+)}$, for a large asymmetry (see Fig. 8.10), the FQHE state becomes more stable than the corresponding state in monolayer graphene.

The Landau level with the label $0_{-1}^{(+)}$ shows a strong dependence of the interaction properties on the parameters of the system. Namely, with increasing bias voltage or
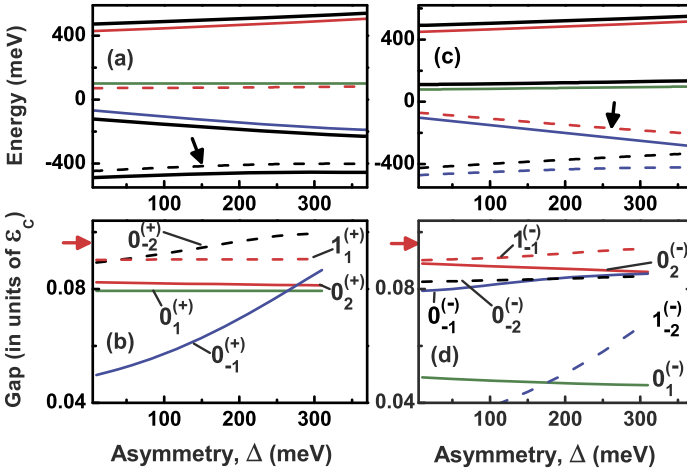
Fig. 8.10 Landau levels of bilayer graphene [panels (**a**) and (**c**)] are shown as a function of the intra-layer asymmetry, Δ. Panels (**b**) and (**b**): the Coulomb gaps of $\frac{1}{3}$-FQHE in corresponding Landau levels. The numbers next to the lines are the labels of the Landau levels. The same types of lines [in panels (**a**) and (**b**) and panels (**c**) and (**d**)] correspond to the same Landau levels. Panels (**a**) and (**b**) correspond to valley K, while panels (**c**) and (**d**) correspond to valley K$'$. The system is characterized by $U = 200$ meV, $\gamma_1 = 400$ meV, and a magnetic field $B = 15$ Tesla. The *arrows* in panels (**a**) and (**c**) show the Landau level with the strongest $\frac{1}{3}$-FQHE. The *arrows* in panels (**b**) and (**d**) indicate the gap of $\frac{1}{3}$-FQHE in the $n = 1$ Landau level of monolayer graphene

intra-layer asymmetry, the gap of the FQHE state and correspondingly its stability strongly increases. At a fixed filling factor of bilayer graphene, this type of behavior can result in the unique experimental observation of a transition from a non-FQHE state at small values of the bias voltage (for example) to a FQHE state at large bias voltages.

The solid black lines in Figs. 8.9–8.11 correspond to the Landau levels without a stable FQHE state. It should be noted that there is also no clear boundary between the Landau levels with and without the FQHE, i.e., between two Landau levels with the FQHE there is a Landau level without FQHE (see Fig. 8.9). This property can be observed experimentally if the FQHE is studied as a function of the filling factor of bilayer graphene while the other parameters of the system are fixed. That means, if one varies the filling factor of bilayer graphene and studies the $\frac{1}{3}$-state at each Landau level then one should be able to observe transitions from the FQHE to no-FQHE state and back to the FQHE state. We should emphasize that this unique phenomenon has never been observed before in conventional two-dimensional systems.

The results illustrated in Fig. 8.9–8.11 are typical for the large inter-layer hopping integral, $\gamma_1 \approx 400$ meV. At smaller values of γ_1, bilayer graphene shows additional features due to anticrossing of the Landau levels as a function of the parameters of the system, i.e., the bias voltage. Such an anticrossing results in a transition of the type, FQHE—no FQHE—FQHE *within the same Landau level* [86]. This be-
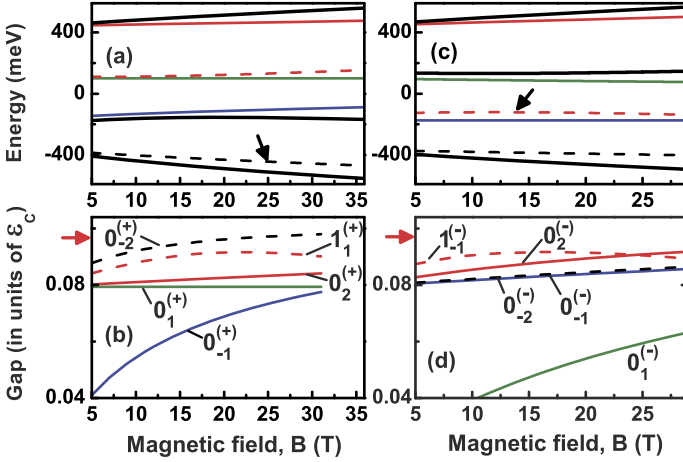
Fig. 8.11 Landau levels of bilayer graphene [panels (**a**) and (**c**)] are shown as a function of the magnetic field. Panels (**b**) and (**b**): the Coulomb gaps of the $\frac{1}{3}$-FQHE in corresponding Landau levels. The numbers next to the lines are the labels of the Landau levels. The same types of lines [in panels (**a**) and (**b**) and panels (**c**) and (**d**)] correspond to the same Landau levels. Panels (**a**) and (**b**) correspond to the valley K, while panels (**c**) and (**d**) correspond to the valley K′. The system is characterized by $\Delta = 150$ meV, $U = 200$ meV, and $\gamma_1 = 400$ meV. The *arrows* in panels (**a**) and (**c**) show the Landau level with the strongest $\frac{1}{3}$-FQHE. The *arrows* in panels (**b**) and (**d**) indicate the gap of the $\frac{1}{3}$-FQHE state in the $n = 1$ Landau level of monolayer graphene

havior is illustrated in Fig. 8.12 for three different values of the inter-layer hopping integral. The actual values of the inter-layer hopping integral depend on the experimental realization of bilayer graphene and is about 400 meV. The anticrossing and the coupling of different Landau levels is more pronounced at small values of γ_1. The anticrossing should be experimentally observable if the filling factor of bilayer graphene is kept fixed and the bias voltage is varied.

For a small inter-layer tunnelling integral and a small bias voltage, some Landau levels in bilayer graphene show strong non-monotonic behavior of the FQHE gap with well-pronounced maxima. This property is illustrated in Fig. 8.13, where the FQHE gap is shown as a function of the inter-layer coupling, γ_1, for two values of the bias voltage, U. The inter-layer coupling can be varied experimentally, for example, by applying a tilted magnetic field, where the parallel component of the magnetic field influences the inter-layer coupling [81]. For small bias voltage, the Landau level $0_1^{(-)}$ has the wave function of the form of (8.33). With variation of the intra-layer tunnelling integral, the wave function (8.33) transforms from the $n = 0$ non-relativistic Landau wave function for small γ_1 to the $n = 1$ monolayer graphene Landau function for $\gamma_1 = 2^{\frac{1}{2}}\hbar v_F/\ell_0$ and finally to the $n = 1$ non-relativistic Landau level function for large γ_1. Therefore the FQHE gap of bilayer graphene in the $0_1^{(-)}$ Landau level is equal to the FQHE gap of the $n = 0$ non-relativistic Landau level for small γ_1 and to the FQHE gap of the $n = 1$ monolayer graphene Landau level for $\gamma_1 = 2^{\frac{1}{2}}\hbar v_F/\ell_0$. This property is illustrated in Fig. 8.13(a), where a strong
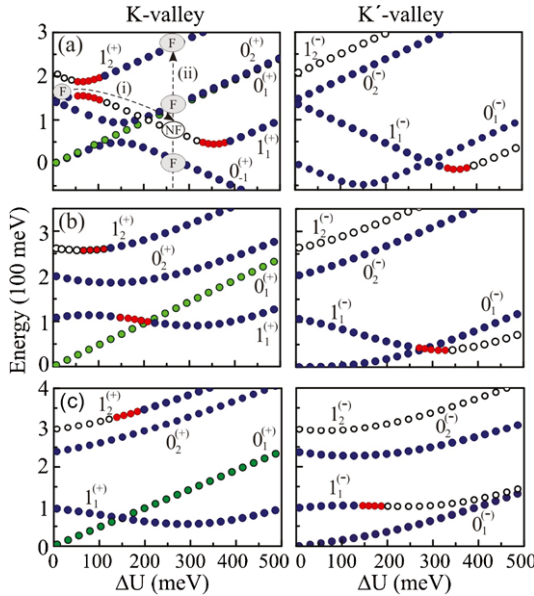
Fig. 8.12 A few lowest Landau levels of the conduction band as a function of the bias potential, U, for different values of inter-layer coupling: (**a**) $\gamma_1 = 30$ meV (**b**) $\gamma_1 = 150$ meV and (**c**) $\gamma_1 = 300$ meV and a magnetic field of 15 Tesla. The intra-layer asymmetry Δ is zero. The *numbers next to the curves* denote the corresponding Landau levels. *Left* and *right columns* correspond to the K and K' valleys, respectively. The Landau levels where the FQHE can be observed are drawn as *blue* and *green filled dots*. The *green dots* correspond to the Landau levels where the FQHE states are identical to that of a monolayer of graphene or a non-relativistic conventional system. The *red dots* represent Landau levels with weak FQHE. The *open dots* correspond to Landau levels where the FQHE is absent. In (**a**), the *dashed lines* labeled by (i) illustrates the transition between FQHE (symbol 'F') and no FQHE (symbol 'NF') states under a constant gate voltage and variable bias potential [86]

non-monotonic behavior of the FQHE gap of the $0_1^{(-)}$ Landau level is shown. The maximum of the FQHE gap at $\gamma_1 \approx 2^{\frac{1}{2}} \hbar v_F / \ell_0$ corresponds to the FQHE gap at $n = 1$ monolayer graphene Landau level.

The above analysis clearly indicates that the interaction properties of biased bilayer graphene depend both on the magnetic field and on the parameters of the system, such as the bias voltage, intra-layer asymmetry, and the inter-layer hopping integral. In each valley there are a few Landau levels which display a strong FQHE, the gap of which depends on the parameters of the bilayer. This dependence can be observed experimentally as transitions between the FQHE and no-FQHE states within the same Landau level when the parameters of the system, e.g., the bias voltage, are changed. Although the FQHE gaps can be controlled by the parameters of the bilayer system, the gaps usually do not exceed the corresponding FQHE gaps in monolayer graphene.
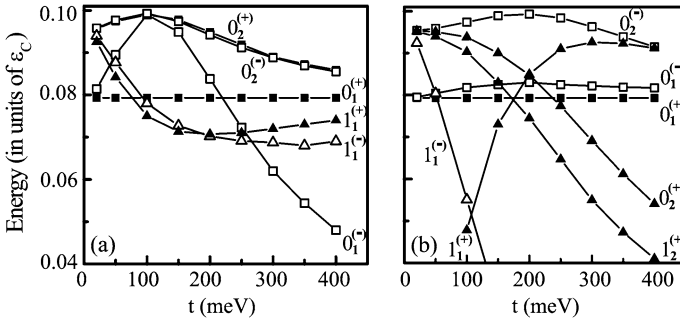
Fig. 8.13 The FQHE gaps shown for different Landau levels. The *labels next to the lines* denote the corresponding Landau levels. (**a**) $U = 10$ meV, and (**b**) $U = 300$ meV. All systems are fully spin polarized and the magnetic field is 15 Tesla. The intra-layer asymmetry Δ is zero [86]

8.3.5 Interacting Electrons in Rotated Bilayer Graphene

Epitaxial graphene [87], which is thermally grown on the C face of the SiC substrate, as well as graphene grown by chemical vapor deposition (CVD) [88], are multilayer films and yet, quite surprisingly display behavior similar to that of a single layer graphene [89]. These systems are known to have a high degree of rotational mis-alignments [90]. Theoretical studies of turbostratic bilayer graphene [91–94] have indicated that in this case the interlayer coupling is suppressed and the systems can be roughly considered as two decoupled layers of graphene, as confirmed by scanning tunneling spectroscopy together with Landau level spectroscopy measurements [95]. At the same time due to the modulated nature [93] of the interlayer transfer integral, these systems show quite rich low-energy physics, which strongly depends on the nature of the commensurate stacking faults [94]. In this section, we will deal with the question: how does the electron-electron interaction manifest itself in a rotated bilayer graphene?

In a misoriented bilayer graphene, one graphene layer is rotated relative to the other layer by an angle θ. We assume that the axis of rotation passes through the atoms of A-sublattices in the two layers (Fig. 8.14). In general, the axis can pass through any point of the bilayer. There is a special type of rotation, called commensurate rotation, which is determined by the condition that the atoms of the two layers are coincident not only at the axis of rotation but also at some other points. The angles corresponding to the commensurate stacking fault are determined from: $\cos\theta = (3q^2 - p^2)/(3q^2 + p^2)$, where $q > p > 0$ are integers [93].

There are two types of commensurate rotations that are distinguished by their symmetry, even or odd, with respect to the sublattice exchange [94]. For the even commensurate stacking fault both A and B sublattice sites of the two layers are coincident at some point, while for the odd stacking fault only A sublattice sites of the two layers are coincident both at the axis of rotation and at some other points. The regular stacking orientations, AA or Bernal, are realized at the following angles: AA-stacking—at angle $\theta = 0$, which corresponds to the even stacking orientation, and Bernal stacking—at angle $\theta = 60°$, which is the odd orientation.

Fig. 8.14 Misoriented graphene bilayer with angle of rotation θ, shown schematically in real space. The axis of rotation passes through atoms of A-sublattice in the two layers. The *black solid dots* and the *red open dots* are the atomic positions in two different layers
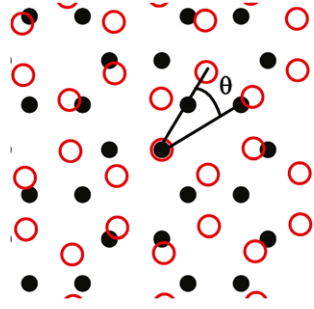
The even and odd stacking faults can also be described in terms of the properties of the reciprocal lattices of the two layers [94]. The reciprocal lattice of a graphene layer consist of K and K' sets of points: $\mathbf{K} + \mathbf{G}_{m,k}$, $\mathbf{K}' + \mathbf{G}_{m,k}$, where $\mathbf{G}_{m,k} = m\mathbf{G}_1 + k\mathbf{G}_2$, m and k are integers, $\mathbf{G}_1 = 2\pi/a(1, \frac{1}{\sqrt{3}})$ and $\mathbf{G}_2 = 2\pi/a(0, \frac{2}{\sqrt{3}})$ are primitive reciprocal lattice vectors, and $\mathbf{K} = 2\pi/a(\frac{1}{3}, \frac{1}{\sqrt{3}})$, $\mathbf{K}' = 2\pi/a(\frac{2}{3}, 0)$. These two sets of points correspond to the two valleys of graphene. Then in terms of the reciprocal lattices, a rotation by an angle θ in real space corresponds to a rotation by an angle θ in reciprocal space about the origin, i.e, (0,0). For an even commensurate stacking fault, the K points of the reciprocal lattices of the two layers are then coincident [94], i.e., $\mathbf{K} + \mathbf{G}_{m,k} = \mathbf{K}(\theta) + \mathbf{G}_{m',k'}(\theta)$, while for the odd stacking fault the K and K' points are coincident, i.e., $\mathbf{K} + \mathbf{G}_{m,k} = \mathbf{K}'(\theta) + \mathbf{G}_{m',k'}(\theta)$ [94]. Here k, m, k', and m' are integer numbers.

Due to the periodic modulation of rotated bilayer graphene at the commensurate angles, the effective interlayer coupling, γ_{eff}, is determined by the Fourier transform of the interlayer potential function at the wave vector $\mathbf{K} + \mathbf{G}_{m,k}$. Then the effective low-energy Hamiltonians of the rotated bilayer at the commensurate condition are given by [94]

$$\mathcal{H}_{even} = \begin{pmatrix} 0 & v_F \pi_- & \gamma_\theta e^{i\phi/2} & 0 \\ v_F \pi_+ & 0 & 0 & \gamma_\theta e^{-i\phi/2} \\ \gamma_\theta^+ e^{i\phi/2} & 0 & 0 & v_F \pi_- \\ 0 & \gamma_\theta^+ e^{i\phi/2} & v_F \pi_+ & 0 \end{pmatrix}, \qquad (8.36)$$

$$\mathcal{H}_{odd} = \begin{pmatrix} 0 & v_F \pi_- & 0 & 0 \\ v_F \pi_+ & 0 & \gamma_\theta & 0 \\ 0 & \gamma_\theta^+ & 0 & v_F \pi_- \\ 0 & 0 & v_F \pi_+ & 0 \end{pmatrix}. \qquad (8.37)$$

The Hamiltonians (8.36) and (8.37) are generalization of the Hamiltonians (8.20) and (8.21) of regular bilayer graphene. Here $\gamma_\theta = \gamma_{eff} e^{i\theta}$ and the phase angle ϕ is determined by the interlayer potential.

For the odd rotated bilayer and for all rotation angles, the Hamiltonian (8.37) is completely identical to the Hamiltonian (8.21) of bilayer graphene with Bernal stacking. The only difference is the magnitude of the interlayer coupling. While for Bernal stacking the interlayer coupling γ_1 is around 400 meV, the coupling

in the rotated bilayer is an order of magnitude smaller, $\gamma_\theta \sim 10$ meV. Therefore, for the effects of the electron-electron interaction and the properties of FQHE, the odd-rotated bilayer behaves similar to bilayer graphene with Bernal stacking and the results of the previous section are applicable to the odd-rotated bilayer.

For the even rotated bilayer the Hamiltonian is similar to the Hamiltonian of bilayer graphene with AA stacking and the interaction properties of the even rotated bilayer become completely identical to the bilayer graphene with AA stacking. The additional phases in the Hamiltonian (8.36) affect the phases of the wave function components, which can be visible in magneto-optics experiments [96], but the pseudopotentials do not depend on these phases and correspondingly on the interlayer coupling. The pseudopotentials for the even rotated bilayer are identical to those of individual graphene layers. Therefore, as far as the FQHE is concerned, the even rotated bilayer can be considered as two decoupled graphene layers for any twist angle.

8.4 Fractional Quantum Hall Effect in Trilayer Graphene

A trilayer graphene consisting of three coupled graphene layers, has a very unique electronic energy spectrum. Within the nearest-neighbor inter-layer coupling approximation, the energy spectrum of trilayer graphene with Bernal stacking consists effectively of decoupled single-layer graphene and the bilayer graphene energy spectra. Therefore the trilayer graphene system allows us to study experimentally both the massless and massive energy spectra within a single system. In a strong perpendicular magnetic field the Landau energy spectrum of trilayer graphene becomes the combination of Landau levels of single-layer and bilayer graphene. This combination exhibits many crossings of the Landau levels as a function of the magnetic field. At the crossing points the Landau levels are highly degenerate. The degeneracy is lifted when the higher-order inter-layer coupling terms are taken into account, resulting in rich properties of quantum Hall effect in trilayer graphene [97, 98].

Novel features of the FQHE should be also expected in trilayer graphene [99]. In what follows, we explore the properties of FQHE in trilayer graphene within the nearest-neighbor inter-layer coupling approximation. The trilayer graphene can be in two main stacking arrangements: the ABA (Bernal) stacking and the ABC stacking, which are schematically shown in Fig. 8.15.

Within the nearest neighbour inter-layer coupling approximation, the Hamiltonian of trilayer graphene is characterized by two parameters alone: the intra-layer, γ_0, and inter-layer, γ_1, tunnelling integrals. In a perpendicular magnetic field the Hamiltonian of trilayer graphene for a single valley, e.g. valley K, takes the form [97, 100]
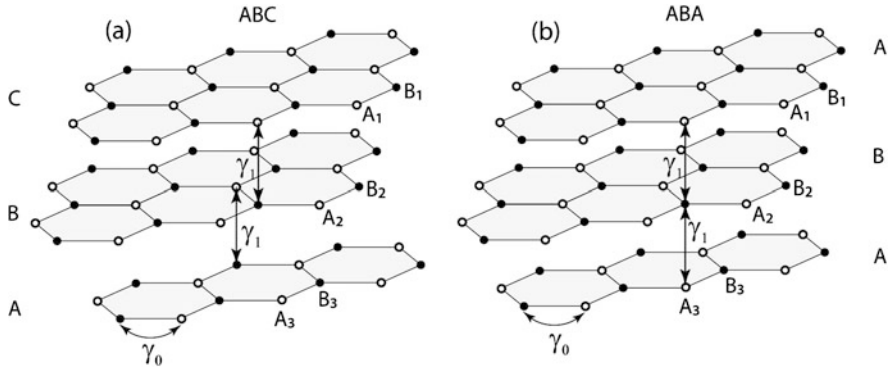
Fig. 8.15 Schematic illustration of two different stacking arrangements of trilayer graphene, consisting of three coupled monolayers of graphene: (**a**) ABC stacking; (**b**) ABA stacking. Each graphene layer consists of two inequivalent sites A and B. The intra-layer and inter-layer hopping integrals are shown by γ_0 and γ_1, respectively

$$
\mathcal{H}^{(ABA)} = \begin{pmatrix}
0 & v_F\pi_- & 0 & 0 & 0 & 0 \\
v_F\pi_+ & 0 & \gamma_1 & 0 & 0 & 0 \\
0 & \gamma_1 & 0 & v_F\pi_- & 0 & \gamma_1 \\
0 & 0 & v_F\pi_+ & 0 & 0 & 0 \\
0 & 0 & 0 & 0 & 0 & v_F\pi_- \\
0 & 0 & \gamma_1 & 0 & v_F\pi_+ & 0
\end{pmatrix}, \tag{8.38}
$$

for the ABA stacking and

$$
\mathcal{H}^{(ABC)} = \begin{pmatrix}
0 & v_F\pi_- & 0 & 0 & 0 & 0 \\
v_F\pi_+ & 0 & \gamma_1 & 0 & 0 & 0 \\
0 & \gamma_1 & 0 & v_F\pi_- & 0 & 0 \\
0 & 0 & v_F\pi_+ & 0 & \gamma_1 & 0 \\
0 & 0 & 0 & \gamma_1 & 0 & v_F\pi_- \\
0 & 0 & 0 & 0 & v_F\pi_+ & 0
\end{pmatrix}, \tag{8.39}
$$

for the ABC stacking. The Landau levels of trilayer graphene can be obtained from the Hamiltonian matrix (8.38) (or (8.39)). The corresponding wave functions are parametrized by the integer n and can be expressed through the non-relativistic Landau level wave functions as

$$
\Psi^{(ABA)} = \begin{pmatrix}
C_1\phi_{n-1,m} \\
C_2\phi_{n,m} \\
C_3\phi_{n,m} \\
C_4\phi_{n+1,m} \\
C_5\phi_{n-1,m} \\
C_6\phi_{n,m}
\end{pmatrix}, \tag{8.40}
$$

for the ABA stacking and

$$\Psi^{(ABC)} = \begin{pmatrix} C_1\phi_{n-1,m} \\ C_2\phi_{n,m} \\ C_3\phi_{n,m} \\ C_4\phi_{n+1,m} \\ C_5\phi_{n+1,m} \\ C_6\phi_{n+2,m} \end{pmatrix}, \tag{8.41}$$

for the ABC stacking. Therefore the Landau wave functions of trilayer graphene are the combinations of n, $n-1$, and $n+1$ non-relativistic Landau functions for the ABA stacking, and n, $n-1$, $n+1$, and $n+2$ non-relativistic Landau functions for the ABC stacking. With the known wave functions, the corresponding form factors of the Haldane pseudopotential can be evaluated from the following expressions

$$\begin{aligned} F_n^{ABA}(q) = & \left(|C_1|^2 + |C_5|^2\right)L_{n-1}\left(q^2/2\right) \\ & + \left(|C_2|^2 + |C_3|^2 + |C_6|^2\right)L_n\left(q^2/2\right) + |C_4|^2 L_{n+1}\left(q^2/2\right), \end{aligned} \tag{8.42}$$

for the ABA stacking and

$$\begin{aligned} F_n^{ABC}(q) = & |C_1|^2 L_{n-1}\left(q^2/2\right) + \left(|C_2|^2 + |C_3|^2\right)L_n\left(q^2/2\right) \\ & + \left(|C_4|^2 + |C_5|^2\right)L_{n+1}\left(q^2/2\right) + |C_6|^2 L_{n+2}\left(q^2/2\right), \end{aligned} \tag{8.43}$$

for the ABC stacking.

The Landau energy spectrum found from the Hamiltonian matrices (8.38) and (8.39) have the following properties:

ABA Stacking The ABA stacking has the unique property that it is completely identical to the combination of the single graphene layer and the bilayer graphene systems. This property follows directly from the Hamiltonian (8.38). Therefore the Landau levels of trilayer graphene consist of the Landau levels of single layer graphene and the Landau levels of bilayer graphene. Within the nearest neighbour inter-layer coupling approximation, considered in the Hamiltonian (8.38) these Landau levels are decoupled. Hence the FQHE in this system should be identical to the FQHE in a single layer graphene and in bilayer graphene.

ABC Stacking For each $n \geq 0$ there are six Landau energy levels with energies [100]

$$\varepsilon_n^{(1)} = \pm\sqrt{2\sqrt{\eta}\cos\left(\frac{\eta}{3}\right) - \frac{\delta_1}{3}} \tag{8.44}$$

$$\varepsilon_n^{(2)} = \pm\sqrt{2\sqrt{\eta}\cos\left(\frac{\eta + 4\pi}{3}\right) - \frac{\delta_1}{3}} \tag{8.45}$$

$$\varepsilon_n^{(3)} = \pm\sqrt{2\sqrt{\eta}\cos\left(\frac{\eta + 2\pi}{3}\right) - \frac{\delta_1}{3}} \tag{8.46}$$

where

$$\cos\eta = \frac{-\frac{\delta_1^3}{27} + \frac{\gamma_1\gamma_2}{6} - \frac{\gamma_3}{2}}{(\frac{\delta_1^2}{9} - \frac{\delta_2}{3})^{3/2}} \tag{8.47}$$

and

$$\delta_1 = -2\gamma_1^2 - 3(1+n)\varepsilon_B^2 \tag{8.48}$$

$$\delta_2 = \gamma_1^4 + 2(1+n)\gamma_1^2\varepsilon_B^2 + (2+6n+3n^2)\varepsilon_B^4 \tag{8.49}$$

$$\delta_3 = -n(n+1)(n+2)\varepsilon_B^6. \tag{8.50}$$

At $n = -1$, there are three Landau levels. One Landau level has zero energy, $\varepsilon = 0$, with the wave function $\Psi^{(ABC)} \propto (0,0,0,-\varepsilon_B\phi_{0,m},0,\gamma_1\phi_{1,m})$. The other two levels have the energies $\varepsilon = \pm\sqrt{\varepsilon_B^2 + \gamma_1^2}$ with the wave functions $\Psi^{(ABC)} \propto (0,0,0,\gamma_1\phi_{0,m},\varepsilon\phi_{0,m},\varepsilon_B\phi_{1,m})$.

At $n = -2$ there is only one Landau level with energy $\varepsilon = 0$ and the wave function $\Psi^{(ABC)} \propto (0,0,0,0,0,\phi_{0,m})$. This Landau level is completely identical to the $n = 0$ non-relativistic Landau level. Therefore, the FQHE at this Landau level should have exactly the same strength as for the $n = 0$ non-relativistic Landau level.

With the known wave functions of the Landau levels of trilayer graphene, we evaluate the form factors and the corresponding pseudopotentials. With these pseudopotentials we then analyse the properties of the FQHE in trilayer graphene. In Fig. 8.16, the lowest Landau levels of trilayer graphene are shown, where the red and blue lines correspond to the Landau levels with a strong FQHE. The strength of the FQHE is characterized by the excitation gap, which are shown in Fig. 8.16 for the filling factor $\nu = \frac{1}{3}$.

For the ABA stacking, the trilayer graphene can be considered as the decoupled system of single layer and bilayer graphene. The blue and red lines correspond to the Landau levels with a strong FQHE of single layer graphene and bilayer graphene, respectively. The strongest FQHE with a gap of $0.09\varepsilon_C$ is observed in the $n = 1$ single graphene layer [see Fig. 8.16(a)]. At the zero energy, the Landau levels of bilayer graphene and the single-layer graphene are degenerate, having the FQHE of the same strength.

For the ABC stacking (see Fig. 8.16), the trilayer graphene cannot be divided into more simple systems. Similar to the ABA stacking there is one Landau level with the strongest FQHE (the gap is $0.09\varepsilon_C$), the gap of which is close to the FQHE gap of the $n = 1$ single layer graphene. The Landau level with zero energy is identical to the $n = 0$ Landau level of the single-layer graphene and the $n = 0$ non-relativistic Landau level. With a few Landau levels showing the strong FQHE, the strength of the FQHE for the ABC stacking does not exceed the strength of the FQHE in a single-layer graphene.
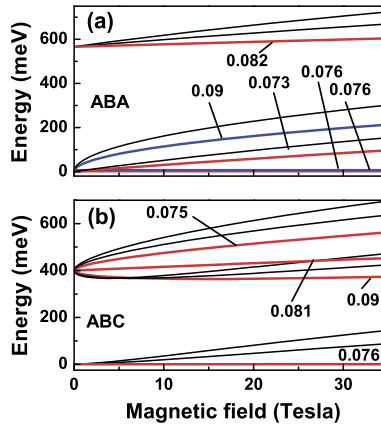
Fig. 8.16 The lowest Landau energy spectra of trilayer graphene shown as the function of the magnetic field for (**a**) ABA and (**b**) ABC stacking. The *red* and *blue lines* correspond to the Landau levels with strong FQHE. The numbers next to the lines are the values of the $\nu = \frac{1}{3}$ FQHE gap (in units of $\varepsilon_C = e^2/\kappa \ell_0$) at the corresponding Landau level. In panel (**a**) the *blue* and *red lines* corresponds to the Landau levels of the single layer and bilayer graphene, respectively

8.5 Some Unique Properties of Interacting Dirac Fermions

In this section, we discuss some of the exotic properties of interacting Dirac fermions. These include the pfaffians in graphene and the FQHE in a topological insulator.

8.5.1 The Pfaffians in Condensed Matter

The vast majority of fractional quantum Hall states observed in the experiments occur at rational filling fractions $\nu = p/q$, with q being an *odd* integer [3, 71]. Further, there have never been any experimental indications that the FQHE would occur at $\nu = \frac{1}{2}$. One also expects that the states in the $(n + 1)$-th lowest Landau level (LLL) should be similar to that at the LLL for $\nu = \frac{1}{2}$, because the lower n Landau levels are then completely filled. The discovery of FQHE in a traditional 2DEG at $\nu = \frac{5}{2}$ in 1987 [101, 102] was therefore a total surprise, for which a proper explanation of the nature of the state has remained elusive ever since [103]. The state was found to be quite robust with a sizeable excitation gap ($\Delta \sim 0.6$ K) and a well-defined plateau. The Laughlin wave function (8.1) is not suitable for this state because at $\nu = \frac{1}{2}$, the appropriate state represents a system of bosons. In order to explain the origin of the corresponding incompressible state, it has been proposed that the ground state of $\nu = \frac{5}{2}$ is described by a Pfaffian [104–107] (or anti-Pfaffian [108, 109]) function. Within this description, the elementary charged excitations have a charge $e^* = e/4$ and obey 'non-abelian' statistics [110, 111]. These unique charged excitations have been recently observed experimentally [112, 113]. Interesting properties

of these quasiparticles, which carry the signatures of Majorana fermions [114–116], have initiated a lot of theoretical interest in the Pfaffian description of the even-denominator FQHE.

The filling factor $\nu = \frac{5}{2} = 2 + \frac{1}{2}$ corresponds to a completely occupied $n = 0$ Landau level with two components of spin and half-filling of the $n = 1$ Landau level. Therefore the Pfaffian state, which is proposed as the incompressible state of $\nu = \frac{5}{2}$, is the ground state of the half-filled $n = 1$ Landau level. It is obtained by operating the Pfaffian factor on the Laughlin state (8.1) at $\nu = \frac{1}{2}$:

$$\Psi_{Pf} = \mathrm{Pf}\left(\frac{1}{z_i - z_j}\right) \prod_{i<j}(z_i - z_j)^2 \exp\left(-\sum_i \frac{z_i^2}{4\ell_0^2}\right), \qquad (8.51)$$

where the positions of the electrons are, as usual, described in terms of complex variable $z = x - iy$ and the Pfaffian factor is defined for any $N \times N$ anisymmetric matrix M_{ij} as [104–107]

$$\mathrm{Pf}\, M_{ij} = \frac{1}{2^{N/2}(N/2)!} \sum_{\sigma \in S_N} \mathrm{sgn}\,\sigma \prod_{l=1}^{N/2} M_{\sigma(2l-1)\sigma(2l)}. \qquad (8.52)$$

Here S_N is the group of permutations of N objects. The Pfaffian factor therefore provides the necessary antisymmetry to the Laughlin state at $\nu = \frac{1}{2}$.

The Pfaffian state is realized at half occupation of the Landau level, i.e., at a filling factor $\nu = \frac{1}{2}$ in a given Landau level, and only for special interaction potentials. The Pfaffian is the exact ground state with zero energy of the electron system at half filling for a special *three-particle* interaction which is non-zero only if all three particles are in close proximity to each other [106, 107]. In spherical geometry with flux quanta $2S$, it means that the three-particle interaction potential is non-zero only if the total angular momentum of the three particles is $3S - 3$, which is described by the following interaction Hamiltonian

$$\mathcal{H}_{int} = \frac{e^2}{\kappa \ell_0} \sum_{i<j<k} P_{ijk}(3S - 3), \qquad (8.53)$$

where $P_{ijk}(L)$ is the three-particle projection operator onto the state with total angular momentum L. For realistic two-particle interactions the $\nu = \frac{1}{2}$ Pfaffian state is not an exact eigenstate. By varying the two-particle interaction function, i.e., the Haldane pseudopotentials, a close proximity of the ground state to the Pfaffian state with an overlap of 99 % can be achieved.

It was shown in Ref. [117] that for traditional non-relativistic systems the Pfaffian (Moore-Read) states can be adiabatically connected to the $\nu = \frac{1}{2}$ Coulomb ground state in the $n = 1$ Landau level by varying the interaction potential from a three-body interaction (8.53) to the Coulomb two-body interaction. However, there is no such connection for the $\nu = \frac{1}{2}$ Coulomb ground state in the $n = 0$ Landau level. The adiabatic connection means that by varying the interaction potential, the system is always kept in the incompressible state with a finite collective excitation gap. This

result illustrates that for the Coulomb interactions, the $\nu = \frac{1}{2}$ state in the $n = 1$ non-relativistic Landau level is in the same topological phase as the Pfaffian state, but the system in the $n = 0$ Landau level does not show any connection to the Pfaffian phase. For the pure Coulomb interaction the overlap of the ground state of the $\nu = \frac{1}{2}$ system in the $n = 1$ Landau level with the Pfaffian function is about 80 %. This overlap can be increased by varying the electron-electron potential strength, for example, by increasing the thickness of the two-dimensional layer [118].

The Pfaffian states are usually studied numerically in the spherical geometry [106, 107, 119]. For a system of N electrons the size of the sphere for which the Pfaffian ground state is realized, is determined by the condition $2S = 2N - 3$, which corresponds to the filling factor $\nu = \frac{1}{2}$ in the thermodynamic limit. For such a system and for the interaction potential of the form of (8.53), the Pfaffian state is an exact ground state with zero energy and finite excitation gap. For the two-particle interaction the interaction potential is characterized by Haldane pseudopotentials (8.2). The proximity of the actual $\nu = \frac{1}{2}$ ground state to the Pfaffian state is most sensitive to the lowest pseudopotentials, V_1, V_3, and V_5.

8.5.2 The Pfaffians in Graphene

The interaction potentials in monolayer and bilayer graphene are different from those of the non-relativistic 2D systems. This can modify the properties of the $\nu = \frac{1}{2}$ state and its proximity to the Pfaffian state in graphene. The numerical analysis in a spherical geometry of a finite-size monolayer graphene system with up to 14 electrons shows that an incompressible $\nu = \frac{1}{2}$ Pfaffian state is unlikely to be found in monolayer graphene [120]. The overlap of the ground state of the $\nu = \frac{1}{2}$ system with the Pfaffian function is less than 0.5 for all Landau levels of the monolayer graphene. The corresponding collective excitation gap is also small.

Interestingly, a very different situation occurs in bilayer graphene. The stability of the $\nu = \frac{1}{2}$ Pfaffian state in bilayer graphene can be greatly enhanced as compared to the non-relativistic system. Here the stability of the incompressible state is determined by the value of the collective excitation gap, which is correlated to the overlap of the ground state and the Pfaffian state. In bilayer graphene there is one 'special' Landau level (for each valley), which is described by (8.33) and has the label $0_{-1}^{(+)}$ in valley K (or $0_1^{(-)}$ in valley K'). Numerical studies [120] in a spherical geometry show that only in this special Landau level the overlap of the ground state with the Pfaffian state and the excitation gap is large. In all other bilayer Landau levels the overlap of the $\nu = \frac{1}{2}$ ground state with the Pfaffian state is found to be small (< 0.6) and those states cannot be described by the Pfaffian.

At the zero bias voltage this special Landau level has zero energy and is degenerate with the level given by (8.32). In addition to this accidental degeneracy, each level has a two-fold valley degeneracy, which makes the zero-energy state four-fold degenerate. At a finite bias voltage this degeneracy is completely lifted and the special Landau level of bilayer graphene can be isolated. In Fig. 8.17, several bilayer

Fig. 8.17 Few LLLs of a
bilayer graphene, shown for
$U = 50$ meV, $\Delta = 0$, and
$t = 400$ meV. The *two solid
red lines* belonging to
different valleys show the
'special' Landau levels where
the $\nu = \frac{1}{2}$ Pfaffian state can
be observed. The *two solid
green lines* show the Landau
levels, which at small
magnetic field, $B \to 0$,
become identical to the $n = 1$
Landau level of the
non-relativistic 2D system
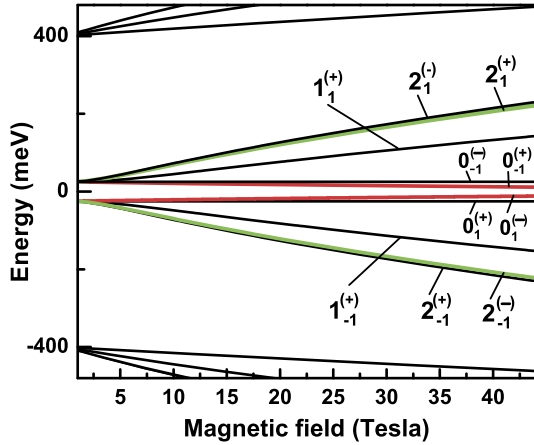
Landau levels are shown at a small bias voltage ($U = 50$ meV) and zero intra-valley asymmetry ($\Delta = 0$). The special Landau levels, $0_{-1}^{(+)}$ and $0_1^{(-)}$, corresponding to two different valleys, are shown by red lines. The interaction potentials and the many-particle properties of these two levels are identical.

From the expression (8.35) for the form factor, F_n, of the Landau level $0_{-1}^{(+)}$ (or $0_1^{(-)}$) we can obtain the following general property: At a small magnetic field, $\gamma_1 \ll \epsilon_B$, the form factor is identical to the form factor of the non-relativistic $n = 1$ Landau level. Therefore in this limit we should expect that the $\nu = \frac{1}{2}$ state is described by the Pfaffian and it is in the same topological phase as the Pfaffian state. By increasing the magnetic field we can change the relation between γ_1 and ϵ_B, which changes the interaction properties of the system and the properties of the $\nu = \frac{1}{2}$ state. Finally, at a very large magnetic field, $\gamma_1 \ll \epsilon_B$, the form factor becomes identical to that of the $n = 0$ non-relativistic system, for which there are no $\nu = \frac{1}{2}$ Pfaffian states. At an intermediate magnetic field there are two possibilities: (i) the excitation gap of the $\nu = \frac{1}{2}$ state and the overlap with the Pfaffian state decrease monotonically with the magnetic field and finally disappear or (ii) the system shows a non-monotonic dependence with the maximum stability, i.e., the maximum gap, at the intermediate magnetic field. Our numerical results show that for bilayer graphene the second situation is indeed realized (see Fig. 8.18 and the discussion below).

In Fig. 8.18, the parameters of the $\nu = \frac{1}{2}$ state are illustrated at the intermediate magnetic field. Here the overlap of the ground state with the Pfaffian state and the corresponding excitation gap are shown. These results clearly indicate that with increasing magnetic field the properties of the system change non-monotonically and for $\gamma_1 = 400$ meV the overlap with the Pfaffian state reaches its maximum at a magnetic field of ~ 10 Tesla. The corresponding excitation gap also reaches its maximum at this point. In dimensionless units the maximum is achieved at $\gamma_1/\epsilon_B \approx 4.89$. Therefore, for smaller values of γ_1 the maximum is achieved at smaller magnetic fields, which is shown in Fig. 8.18 for $\gamma_1 = 300$ meV. The overlap with the Pfaffian state at the maximum point is ≈ 0.92, which is a major improvement over the

Fig. 8.18 (**a**) Overlap of the exact many-particle ground state with the Pfaffian function. (**b**) Collective excitation gap of the $\nu = \frac{1}{2}$ state. The results are for $N = 14$, $2S = 25$, and $U = 0$, $\Delta = 0$. The *black* and *red lines* correspond to $\gamma_1 = 400$ meV and 300 meV, respectively. The results are shown for of the $\nu = \frac{1}{2}$ system at 'special' Landau levels marked by red lines in Fig. 8.17
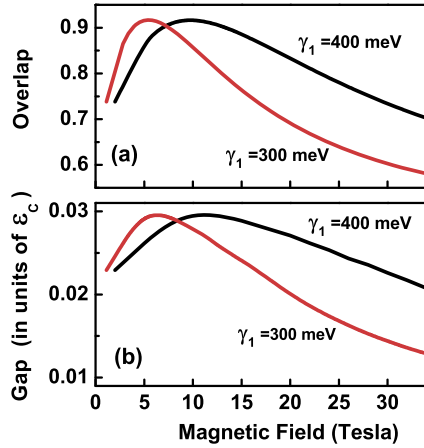
non-relativistic system (~ 0.75, which is the value at zero magnetic field limit in Fig. 8.18).

Within this picture the magnetic field should be considered as the parameter which adiabatically changes the interaction Hamiltonian from the $n = 1$ non-relativistic system to the bilayer system at the special Landau level, $0_{-1}^{(+)}$. These changes are adiabatic since the gap remains non-zero and large. Therefore, we conclude that the $\nu = \frac{1}{2}$ state at the special bilayer Landau level is in the same topological phase as the $\nu = \frac{1}{2}$ state in the $n = 1$ non-relativistic Landau level and correspondingly as the Pfaffian state. At the same time the overlap with the Pfaffian state and the excitation gap is larger in bilayer graphene (at $B \sim 10$ Tesla) than in the non-relativistic system. Therefore, bilayer graphene provides the more stable Pfaffian state.

At a large magnetic field the bilayer system, at the special Landau level, $0_{-1}^{(+)}$, becomes close to the $n = 0$ non-relativistic Landau level, the overlap with the Pfaffian state becomes small, the excitation gap becomes small, and the $\nu = \frac{1}{2}$ state finally becomes compressible. This dependence on the magnetic field opens up interesting possibilities to investigate the stability and appearance and disappearance of the $\nu = \frac{1}{2}$ Pfaffian state in a single Landau level of bilayer graphene. Although the Pfaffian state becomes unstable only at large magnetic fields, this property strongly depends on the value of the hopping integral. At smaller hopping integrals the magnetic field range of stability of the Pfaffian state shrinks. For example, at $t = 300$ meV the Pfaffian state is expected to be unstable at $B \sim 40$ Tesla (note the suppression of the FQHE gap with increasing magnetic field in Fig. 8.18). The dependence of the properties of the $\nu = \frac{1}{2}$ state on the bias voltage is weak within the broad range of U [120].

In bilayer graphene there is another set of Landau levels, which are shown by green lines in Fig. 8.17 and are labelled as $2_1^{(+)}$ for valley K and $2_{-1}^{(-)}$ for valley K'. These Landau levels have the following property. At a finite bias voltage and a small magnetic field, the corresponding Landau level wave functions are described
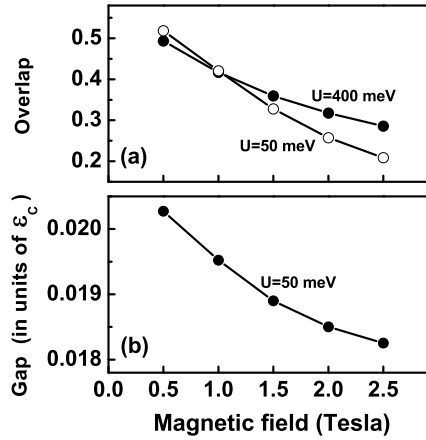
by the $n = 1$ non-relativistic Landau wave functions, $(0, \phi_{1,m}, 0, 0)$. Therefore in this limit the interaction potentials become identical to the interaction potentials of the non-relativistic system in the $n = 1$ Landau level. Then the $\nu = \frac{1}{2}$ Pfaffian state should be realized in the bilayer Landau level $2_1^{(+)}$ $(2_{-1}^{(-)})$ for small values of the magnetic field. With increasing magnetic field the interaction potentials are modified which should influence the properties of the $\nu = \frac{1}{2}$ state. In Fig. 8.19, we present the magnetic field dependence of the parameters of the $\nu = \frac{1}{2}$ state in the Landau level $2_1^{(+)}$ $(2_{-1}^{(-)})$. Evidently, in this case with an increasing magnetic field the overlap with the Pfaffian state and the excitation gap are strongly suppressed. Therefore in this bilayer Landau level the $\nu = \frac{1}{2}$ Pfaffian state cannot be realized.

The stability of the $\nu = \frac{1}{2}$ ground state and its proximity to the Pfaffian state can also be analyzed in terms of the general dependence of the Haldane pseudopotentials, V_m, on the relative angular momentum, m. The $\nu = \frac{1}{2}$ Pfaffian state is most sensitive to the following parameters of the pseudopotential: V_1/V_5 and V_3/V_5 [117]. These parameters depend on the strength of the magnetic field. By varying the magnetic field, we introduce an adiabatic transition of the pseudopotentials from one set to another. Such a transition can be shown as a line in the (V_1/V_5)–(V_3/V_5) plane (see Fig. 8.20). That line connects the initial point at $B = 0$ to the final point, corresponding to a large magnetic field, $B = \infty$. In Fig. 8.20, three regions which were identified in Ref. [117] are shown: (i) region of large overlap of the $\nu = \frac{1}{2}$ ground state with the Pfaffian function and the largest excitation gap and correspondingly the most stable $\nu = \frac{1}{2}$ Pfaffian state. (ii) That region is surrounded by the region of less stable Pfaffian state. (iii) The region of compressible states, i.e., with zero excitation gap.

The red line in Fig. 8.20 (a) corresponds to the special bilayer Landau level $0_{-1}^{(+)}$ $(0_1^{(-)})$ (Fig. 8.17). In this Landau level the $\nu = \frac{1}{2}$ bilayer graphene system at the initial and final points are identical to the non-relativistic 2D systems in the first $(n = 1)$ and zero $(n = 0)$ Landau levels, respectively. For the intermediate magnetic
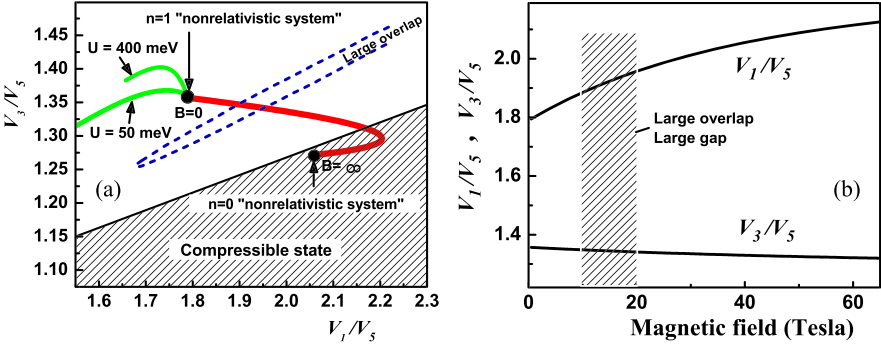
Fig. 8.20 (**a**) The trajectory of the inter-electron interaction pseudopotential with varying magnetic field, shown by a *solid red line* in the plane (V_1/V_5)–(V_3/V_5) for the 'special' bilayer Landau levels $0_1^{(-)}$ and $0_{-1}^{(+)}$. The corresponding Landau levels are marked by a red line in Fig. 8.17. The *green lines* depict the trajectory of the interaction potential corresponding to the Landau levels $2_{-1}^{(-)}$ and $2_1^{(+)}$, marked by green lines in Fig. 8.17. The initial point of the trajectory (at $B = 0$) corresponds to the non-relativistic system in the $n = 1$ Landau level, while the final point (at $B = \infty$) corresponds to the non-relativistic system in the $n = 0$ Landau level. The *shaded region* illustrates the compressible $\nu = \frac{1}{2}$ state, while the *blank region* corresponds to the incompressible $\nu = \frac{1}{2}$ state (Ref. [117]). The crossing of the boundary between the compressible and incompressible states occurs at $B \sim 100$ Tesla for the hopping integral $\gamma_1 = 400$ meV. The *blue dashed line* shows the region of large overlap with the Pfaffian state (Ref. [117]). (**b**) Ratios of the pseudopotentials at two values of the angular momentum are shown as a function of the magnetic field for two 'special' Landau levels $0_1^{(-)}$ and $0_{-1}^{(+)}$. The *dashed region* corresponds to a large overlap of the ground state with the Pfaffian function and also a large excitation gap

field the line goes through the region of most stable Pfaffian state. Therefore with an increasing magnetic field, the $\nu = \frac{1}{2}$ bilayer graphene system in the special Landau level transforms from a $\nu = \frac{5}{2}$ non-relativistic state (at small values of B) to a more stable incompressible state with a large overlap and a large gap, and finally to a compressible state (at a large magnetic field). This behavior is consistent with the result shown in Fig. 8.18, where the large excitation gap is realized at a finite magnetic field. For the hopping integral $t = 400$ meV, the transition from the incompressible to a compressible $\nu = \frac{1}{2}$ state occurs at $B \sim 100$ Tesla. In Fig. 8.20(b) the dependences of both parameters (V_1/V_5) and (V_3/V_5) on the magnetic field are shown for the bilayer Landau level $0_{-1}^{(+)}$. These dependences correspond to the red line in Fig. 8.20(a). The dashed region shows the region of the stable $\nu = \frac{1}{2}$ ground state with a large excitation gap and a large overlap with the Pfaffian state. This region is realized at a finite magnetic field, $B \sim 10$ Tesla, which is consistent with the results of Fig. 8.18.

The green lines in Fig. 8.20 correspond to the Landau level $2_1^{(+)}$ ($2_{-1}^{(-)}$) (Fig. 8.17). The results clearly show that with increasing magnetic field and for all values of U and Δ, the $\nu = \frac{1}{2}$ system becomes less stable by having a smaller excitation gap, which support the results shown in Fig. 8.19.

Therefore, the incompressible $\nu = \frac{1}{2}$ Pfaffian state can actually be found in a bilayer graphene in one of the Landau levels. The properties of this state strongly depend on the magnetic field strength. With increasing magnetic field the graphene system at this special Landau level shows a transition from the incompressible to a compressible state with increasing magnetic field. At a finite magnetic field the Pfaffian state in bilayer graphene becomes more stable with the larger excitation gap than its counterpart in non-relativistic 2D electron systems.

8.5.3 Interacting Dirac Fermions on the Surface of a Topological Insulator

The relativistic dispersion relation, observed in monolayer graphene, is also realized in special insulators with topologically protected surface states [121, 122]. Those states in topological insulators are gapless with a linear (relativistic) dispersion relation similar to the energy spectra of graphene. Therefore the properties of the surface states of topological insulators are expected to be similar to the properties of graphene. Experimentally the topological insulator has been realized in $Bi_{1-x}Sb_x$ and Bi_2Se_3 materials, containing a *single Dirac cone* on the surface [123, 124].

In an external magnetic field the properties of surface Landau levels of a topological insulator are similar to those of Landau levels in graphene [125, 126]. Although the low-energy dynamics of the surface states is similar to graphene, there is however, an important difference between these two systems. While the electronic states of graphene are strictly two-dimensional and are localized within a single graphene plane, the surface states in a topological insulator have a finite width in the growth direction. The finite width of the surface states in topological insulators modifies the electron-electron interaction potential which in turn, modifies the properties of the FQHE states. In traditional (non-relativistic) electron systems, an increase in the width of the 2D layer causes a reduction of the FQHE gaps and hence a reduction of the stability of the corresponding incompressible states. Therefore, we should expect that the FQHE gaps in a topological insulator would be smaller than those in graphene.

To analyze the properties of the FQHE in the surface states of a topological insulator (TI), we start with the low-energy effective Hamiltonian introduced in Ref. [127, 128]. The Hamiltonian has the matrix form of size 4×4 and is given by

$$\mathcal{H}_{TI} = \begin{pmatrix} \epsilon(\mathbf{p}) + M(\mathbf{p}) & (A_1/\hbar)p_z & 0 & (A_2/\hbar)p_- \\ (A_1/\hbar)p_z & \epsilon(\mathbf{p}) - M(\mathbf{p}) & (A_2/\hbar)p_- & 0 \\ 0 & (A_2/\hbar)p_+ & \epsilon(\mathbf{p}) + M(\mathbf{p}) & -(A_1/\hbar)p_z \\ (A_2/\hbar)p_+ & 0 & -(A_1/\hbar)p_z & \epsilon(\mathbf{p}) - M(\mathbf{p}) \end{pmatrix}, \quad (8.54)$$

where $\epsilon(\mathbf{p}) = C_1 + (D_1/\hbar^2)p_z^2 + (D_2/\hbar^2)(p_x^2 + p_y^2)$, $M(\mathbf{p}) = M_0 - (B_1/\hbar)p_z^2 - (B_2/\hbar^2)(p_x^2 + p_y^2)$. Here for the Bi_2Se_3 topological insulator the material constants are $A_1 = 2.2$ eV Å, $A_2 = 4.1$ eV Å, $B_1 = 10$ eV Å^2, $B_2 = 56.6$ eV Å^2,

$C_1 = -0.0068$ eV, $D_1 = 1.3$ eV Å^2, $D_2 = 19.6$ eV Å^2, and $M_0 = 0.28$ eV. The topological insulator film has a finite thickness of L_z, where the axis z is a trigonal axis of Bi_2Se_3 with three-fold rotational symmetry. We assume that the two surfaces of the film are at $z = 0$ and $z = L_z$. The four-component wave functions corresponding to the Hamiltonian (8.54) determine the amplitudes of the wave functions at the positions of Bi and Se atoms: $(Bi_\uparrow, Se_\uparrow, Bi_\downarrow, Se_\downarrow)$, where the arrows indicate the electron spin directions.

The external magnetic field is introduced along the z-direction which results in Landau quantization of the electron motion in the x–y plane. The corresponding Landau levels, which include both the surface and bulk Landau levels, can be found from the Hamiltonian matrix by replacing the x and y components of the momentum by the generalized momentum [129] and introducing the Zeeman energy, $\Delta_z = \frac{1}{2} g_s \mu_B B$. Here $g_s \approx 8$ is the effective g-factor of surface states [128, 130] and μ_B is the Bohr magneton. The Landau levels are characterized by an integer index n with the corresponding wave functions

$$\Psi_n^{(TI)} = \begin{pmatrix} \chi_n^{(1)}(z)\phi_{|n|-1,m} \\ \chi_n^{(2)}(z)\phi_{|n|-1,m} \\ i\chi_n^{(3)}(z)\phi_{|n|,m} \\ i\chi_n^{(4)}(z)\phi_{|n|,m} \end{pmatrix}, \tag{8.55}$$

for $n > 0$ and

$$\Psi_n^{(TI)} = \begin{pmatrix} 0 \\ 0 \\ i\chi_n^{(3)}(z)\phi_{|n|,m} \\ i\chi_n^{(4)}(z)\phi_{|n|,m} \end{pmatrix}, \tag{8.56}$$

for $n = 0$. The functions $\chi_n^{(i)}(z)$ satisfy the following eigenvalue equations

$$\varepsilon\chi_n^{(1)}(z) = (\epsilon_{z,n} + M_{z,n} + \Delta_z)\chi_n^{(1)}(z)$$
$$+ iA_1\frac{d\chi_n^{(2)}(z)}{dz} - \frac{\sqrt{2(n+1)}}{\ell_0}A_2\chi_n^{(4)}(z) \tag{8.57}$$

$$\varepsilon\chi_n^{(2)}(z) = (\epsilon_{z,n} - M_{z,n} + \Delta_z)\chi_n^{(2)}(z)$$
$$+ iA_1\frac{d\chi_n^{(1)}(z)}{dz} - \frac{\sqrt{2(n+1)}}{\ell_0}A_2\chi_n^{(3)}(z) \tag{8.58}$$

$$\varepsilon\chi_n^{(3)}(z) = (\epsilon_{z,n+1} + M_{z,n+1} - \Delta_z)\chi_n^{(3)}(z)$$
$$- iA_1\frac{d\chi_n^{(4)}(z)}{dz} - \frac{\sqrt{2(n+1)}}{\ell_0}A_2\chi_n^{(2)} \tag{8.59}$$

$$\varepsilon\chi_n^{(4)}(z) = (\epsilon_{z,n+1} - M_{z,n+1} - \Delta_z)\chi_n^{(4)}(z)$$
$$- iA_1\frac{d\chi_n^{(3)}(z)}{dz} - \frac{\sqrt{2(n+1)}}{\ell_0}A_2\chi_n^{(1)}, \tag{8.60}$$

where $\epsilon_{z,n} = C_1 + D_2\frac{2n+1}{\ell_0^2} - D_1\frac{d^2}{dz^2}$ and $M_{z,n} = M_0 - B_2\frac{2n+1}{\ell_0^2} - B_1\frac{d^2}{dz^2}$. The solution of the system of equations (8.57)–(8.60) determines the Landau level energy spectra and the corresponding wave functions. We are interested only in the surface
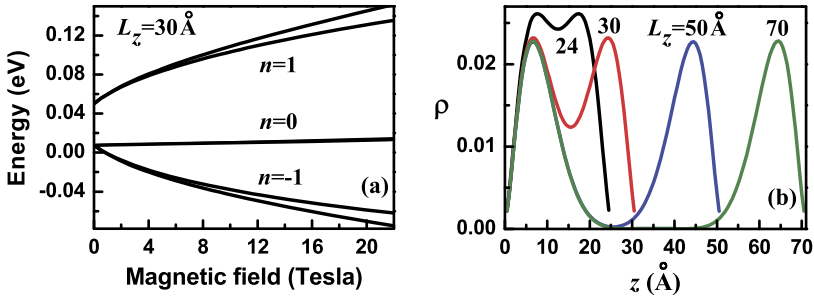
Fig. 8.21 (**a**) The lowest surface Landau levels of a TI film are shown at a film thickness of $L_z = 30$ Å. For each n there are two LLs of the TI film, belonging to the two surfaces of the film. (**b**) The electron density along the z axis for one of the $n = 1$ Landau levels and for different values of the thickness, L_z, of the Bi_2Se_3 film. The *numbers next to the lines are* the values of L_z. The magnetic field is at 15 Tesla

Landau levels. These Landau levels are separated from the bulk Landau levels by finite energy gaps and the wave functions of the surface Landau levels are localized near the surface of the topological insulator. We assume that the wave functions χ_n satisfy open boundary conditions (zero values) at the two surfaces of the TI film, which correspond to a suspended TI film. The substrate can be taken into account by modification of the boundary conditions.

For a topological insulator film there are two surfaces which results in two sets of surface Landau levels. For thick films the separation between the Landau levels of the two surfaces is large and the levels with the same n are degenerate. The wave functions of the surface Landau levels have a finite width and therefore for small thicknesses of the films, the wave functions of the two surfaces of the Bi_2Se_3 film overlap. This results in inter-Landau level coupling which lifts the degeneracy of the Landau levels of the two surfaces. In Fig. 8.21(a) the lowest energy surface Landau levels with indices $n = 0$ and $n = 1$ are shown for a Bi_2Se_3 topological insulator film of thickness $L_z = 30$ Å. For each n there are two Landau levels of the two surfaces of the film. The degeneracy of the Landau levels is lifted due to the finite film thickness and the finite inter-Landau level coupling. This coupling is more pronounced at a small film thickness due to the larger overlap of the corresponding wave functions [Fig. 8.21(b)] where results for four film thicknesses are shown. For small L_z, the wave functions of the two surface states have a large overlap and a large value within the whole topological insulator film, which results in a strong inter-Landau level coupling. For large L_z, the surface Landau levels are localized at the two surfaces of the film, resulting in a weak inter-Landau level coupling. The strong inter-Landau level coupling lifts the degeneracy of the surface Landau levels and changes the corresponding wave functions. The most important effect is how this coupling affects the contributions of the n and $n - 1$ non-relativistic Landau functions, $\phi_{|n|,m}$ and $\phi_{|n|-1,m}$ (see (8.55)), to the Landau wave functions of the surface states. For the $n = 0$ surface Landau level this is not important since only $n = 0$ non-relativistic Landau functions enter in the expression (8.56), while for the
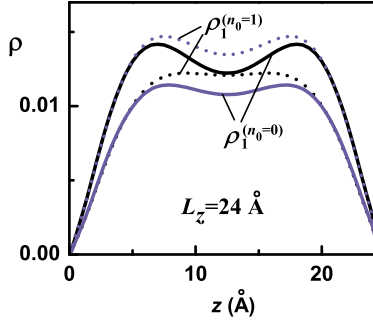
Fig. 8.22 The electron densities $\rho_1^{(n=1)}(z)$ and $\rho_1^{(n=0)}(z)$ of two $n=1$ Landau levels for film thickness of $L_z = 24$ Å. The *black (solid and dotted) lines* and *blue (solid and dotted) lines* correspond to two $n=1$ Landau levels. The densities $\rho_1^{(n=1)}(z)$ and $\rho_1^{(n=0)}(z)$ show the occupations of the $n=1$ and $n=0$ non-relativistic Landau level functions, respectively

$n=1$ surface state both the $n=1$ and $(n-1)=0$ non-relativistic Landau functions determine the properties of the topological insulator state. To show the effect of the inter-Landau level coupling on the wave functions we present in Fig. 8.21 the electron densities

$$\rho_1^{(n_0=1)}(z) = \left|\chi_{n=1}^{(3)}(z)\right|^2 + \left|\chi_{n=1}^{(4)}(z)\right|^2, \tag{8.61}$$

$$\rho_1^{(n_0=0)}(z) = \left|\chi_{n=1}^{(1)}(z)\right|^2 + \left|\chi_{n=1}^{(2)}(z)\right|^2, \tag{8.62}$$

which determine the contribution of the $n_0 = 1$ and $n_0 = 0$ non-relativistic Landau functions to the corresponding surface Landau levels. The results are shown in Fig. 8.21(b) for two $n=1$ surface Landau levels, which are coupled due to inter-Landau level coupling. Figure 8.22 shows clearly that one of the $n=1$ surface Landau levels has a larger contribution from the $n_0 = 0$ non-relativistic Landau function, $\phi_{n_0=0,m}$, while the other $n=1$ surface Landau level has a large contribution from the $n_0 = 1$ non-relativistic Landau function, $\phi_{n_0=1,m}$.

With the known wave functions of the surface Landau levels (8.55)–(8.56), the Haldane pseudopotentials, (8.2), can be readily evaluated from the following expression

$$V_m^{(n=0)} = \int_0^\infty \frac{dq}{2\pi} q V(q) F_{1,1}(q) L_n^2\left(\frac{q^2}{2}\right) L_m(q^2) e^{-q^2}, \tag{8.63}$$

for $n = 0$, and

$$
\begin{aligned}
V_m^{(n)} = \int_0^\infty \frac{dq}{2\pi} q V(q) \frac{1}{4} \bigg[& F_{1,1}(q) L_n^2\left(\frac{q^2}{2}\right) \\
& + 2F_{1,2}(q) L_n\left(\frac{q^2}{2}\right) L_{n-1}\left(\frac{q^2}{2}\right) \\
& + F_{2,2}(q) L_{n-1}^2\left(\frac{q^2}{2}\right) \bigg] L_m(q^2) e^{-q^2},
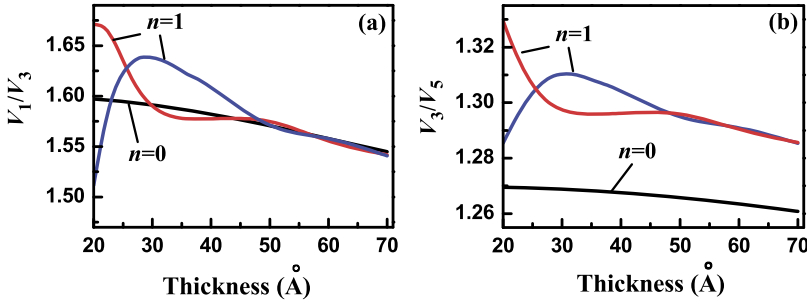\end{aligned}
\tag{8.64}
$$

Fig. 8.23 The ratios of pseudopotentials, (V_1/V_3) (panel (**a**)) and (V_3/V_5) (panel (**b**)), for the surface Landau levels of a Bi_2Se_3 topological insulator at two odd relative angular momenta shown as a function of the thickness of the topological insulator film. The ratios are shown for the $n = 0$ and two $n = 1$ surface Landau levels of the topological insulator

for $n > 0$. Here the form factors $F_{i,j}(q)$ are evaluated from,

$$F_{1,1}(q) = \int dz_1 dz_2 \rho_n^{(n_0=n)}(z_1)\rho_n^{(n_0=n)}(z_2)e^{-|z_1-z_2|q},$$

$$F_{1,2}(q) = \int dz_1 dz_2 \rho_n^{(n_0=n)}(z_1)\rho_n^{(n_0=n-1)}(z_2)e^{-|z_1-z_2|q},$$

$$F_{2,2}(q) = \int dz_1 dz_2 \rho_n^{(n_0=n-1)}(z_1)\rho_n^{(n_0=n-1)}(z_2)e^{-|z_1-z_2|q},$$

where $\rho_n^{(n_0=n)}(z) = |\chi_n^{(3)}(z)|^2 + |\chi_n^{(4)}(z)|^2$ and $\rho_n^{(n_0=n-1)}(z) = |\chi_n^{(1)}(z)|^2 + |\chi_n^{(2)}(z)|^2$ determine the occupation of $n_0 = n$-th and $n_0 = n - 1$-th non-relativistic LLs for the topological insulator surface Landau level with index n.

The mixture of surface Landau levels has a strong effect on the pseudopotentials, which is visible only at a small thickness of the film and for $n = 1$ Landau levels [see (8.63) and (8.64)]. The stability of the incompressible states (i.e., the gaps of the FQHE states) depends on how fast the pseudopotentials decreases with increasing relative angular momentum, m. In Fig. 8.23, the ratios of the two nearest odd pseudopotentials, (V_1/V_3) and (V_3/V_5), are shown as the function of the thickness of the film for the $n = 0$ and $n = 1$ surface Landau levels. For the $n = 0$ Landau level the ratios of the pseudopotentials monotonically decrease with the thickness, L_z. This monotonic dependence shows that the $n = 0$ surface Landau level does not depend on the mixture of two surface states and the reduction is due to the increase of the width of the surface wave functions in the z-direction [Fig. 8.21(b)]. For two $n = 1$ surface Landau levels there is a different dependence on the L_z. For a small thickness the inter-Landau level coupling is large, which results in a strong nonmonotonic dependence of the pseudopotential ratios on L_z. For one of the $n = 1$ Landau levels the pseudopotential ratios have a well pronounced maximum. For a large thickness of the topological insulator film, the inter-Landau level coupling is weak and the pseudopotentials monotonically decrease with L_z, which is similar to that of the $n = 0$ Landau level and is due to the increase of the width of the surface wave functions in the z-direction. For a large thickness of the topological insulator film, the ratio of the first two pseudopotentials, V_3/V_1, becomes the same for all
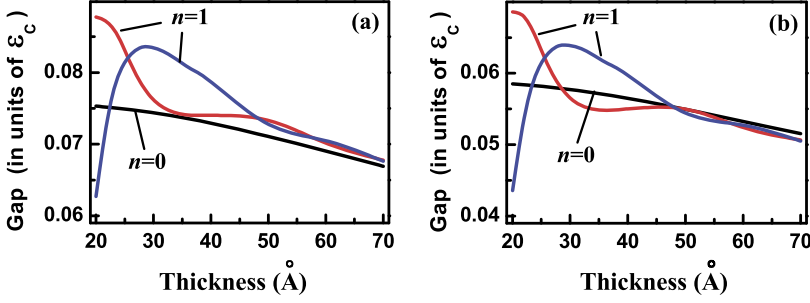
Fig. 8.24 (**a**) The $\nu = \frac{1}{3}$ FQHE gap shown for different Landau levels of a topological insulator film as a function of the film thickness. The FQHE gaps were evaluated numerically for a finite-size system of $N = 9$ electrons and flux quanta $2S = 24$. (**b**) The $\nu = \frac{2}{5}$ FQHE gap is shown for different Landau levels of the topological insulator film as a function of the film thickness. The FQHE gaps were evaluated numerically for a finite-size system of $N = 10$ electrons and the flux quanta $2S = 21$. The magnetic field is 15 Tesla and the energy is shown in units of the Coulomb energy, $\varepsilon_C = e^2/\kappa \ell_0$

Landau levels. This fact suggests that for large L_z ($L_z > 50$ Å) the FQHE gaps are almost the same in the $n = 0$ and $n = 1$ Landau levels.

With the known pseudopotentials the energy spectra of the $\nu = \frac{1}{3}$ and $\nu = \frac{2}{5}$ FQHE systems are evaluated numerically in the spherical geometry. The corresponding energy gaps are shown in Fig. 8.24(a) and (b), as a function of film thickness [131]. The L_z dependence of the energy gaps is very similar to the L_z dependence of the ratio of the pseudopotentials of the energy gaps at the corresponding LLs (see Fig. 8.23). For a small thickness, the non-monotonic dependence for the $n = 1$ Landau levels is due to the inter-Landau mixture, while for a large thickness, the FQHE gaps monotonically decrease with the thickness due to the increase of the width in the z-direction of the surface wave functions. The FQHE gaps in the $n = 1$ and $n = 0$ Landau levels become almost the same for large thicknesses of the film.

Experimentally it would be easier to study the dependence of the FQHE gaps on the parameters of the system for a given thickness of the film by varying the strength of the external magnetic field. In Fig. 8.25, we show the dependence of the $\nu = \frac{1}{3}$ FQHE gap on the magnetic field for two different films with a small thickness, $L_z = 25$ Å, and a large thickness, $L_z = 50$ Å. The results presented in Figs. 8.24 and 8.25 are shown for actual values of the film thicknesses and the magnetic field. Within the inter-Landau level mixture, the properties of the TI film are determined by a dimensionless parameter which is the dimensionless thickness of the film, expressed in units of the magnetic length. Therefore with increasing magnetic field the magnetic length decreases, and the dimensionless thickness increases. Then without any inter-Landau mixture we would expect a monotonic decrease of the excitation gaps with magnetic field due to the increase of the dimensionless width of the surface wave functions. For the small thickness of 25 Å, which is about two quintuple layers of Bi_2Se_3 [Fig. 8.25(a)], the inter-Landau coupling is strong. As a result the FQHE gap at one of the $n = 1$ Landau levels increases monotonically with magnetic field, while the other $n = 1$ Landau level displays a monotonic decrease of the gap
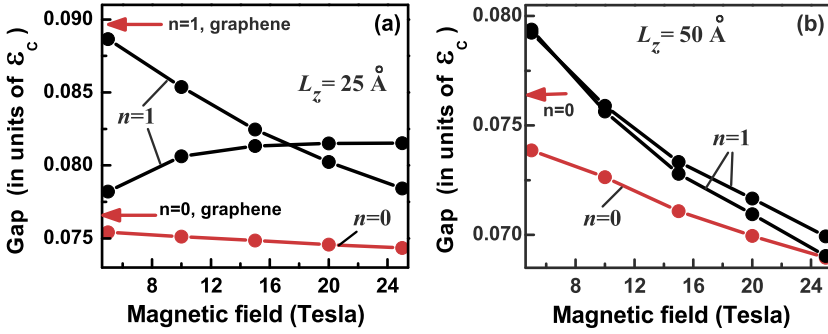
Fig. 8.25 The $\nu = \frac{1}{3}$ FQHE gap as a function of the magnetic field shown for different Landau levels of a topological insulator film: two $n = 1$ LLs (*black lines*) and one $n = 0$ LL (*red line*). The thickness of the film is (**a**) $L_z = 25$ Å and (**b**) $L_z = 50$ Å. The *red arrows* show the FQHE gaps in the $n = 0$ and $n = 1$ Landau levels of graphene. The FQHE gaps were evaluated numerically for a finite-size system of $N = 9$ electrons and flux quanta $2S = 24$. The energy is shown in units of the Coulomb energy, $\varepsilon_C = e^2/\kappa \ell_0$

with magnetic field, B. An experimental observation of the monotonic increase of the FQHE gaps with magnetic field would be a direct manifestation of the strong inter-Landau level coupling.

For a large film thickness of 50 Å, i.e., five quintuple layers of Bi_2Te_3 [Fig. 8.25(b)], the inter-Landau level coupling is weak and we see a monotonic decrease of the FQHE gaps with magnetic field for all Landau levels. This is due to the increase of the dimensionless width of the surface Landau level wave functions. For the $n = 0$ Landau levels, which are not affected by the Landau level coupling, a monotonic decrease with magnetic field, B, is visible for both small and large thicknesses of the film. The results shown in Fig. 8.25 also illustrate the fact that the FQHE gaps in a topological insulator are less than the maximum FQHE gap that is expected in graphene in the $n = 1$ Landau level.

The FQHE can indeed be observed on the surface Landau levels of a topological insulator. The strength of the FQHE, which is characterized by the value of the excitation gap, has non-trivial dependence on the thickness of the film. For a small thickness of the topological insulator film, the inter-Landau level coupling and the mixture of the Landau levels are strong, which results in a non-monotonic dependence, with a well-pronounced maximum of the FQHE gaps on the thickness of the film, in the $n = 1$ Landau levels. For a large thickness of the film, when the inter-Landau level coupling is small, the FQHE gaps monotonically decrease with the thickness, which is to an increase of the width of the surface Landau levels. The effect of the inter-Landau level coupling on the $n = 0$ surface states is very weak. As a result, for the $n = 0$ Landau levels the FQHE gaps monotonically decrease with the thickness for all values of L_z. In general, for a finite thickness of the topological insulator films, the FQHE gaps are the largest in the $n = 1$ Landau levels, which is similar to the case of a monolayer graphene. At a large enough thickness of the film, $L_z > 50$ Å, the gaps of FQHE states in the $n = 0$ and $n = 1$ Landau levels become comparable (Fig. 8.24). Experimental observation of these theoretical predictions,

just as in the case of graphene [69, 72, 77] would be an important advancement in our understanding of this unique state of matter. The possibility of a controllable growth of the Bi_2Se_3 nanofilm in a wide range of one quintuple layer (10 Å) to 15 quintuple layer (150 Å) has been demonstrated in [132]. This indeed opens up the interesting possibility to study the FQHE in Bi_2Se_3 films of different thicknesses.

8.6 Conclusions

We have briefly reviewed the rich physics exhibited by interacting electrons in monolayer and bilayer graphene in the quantum Hall effect regime. The behavior of massless Dirac fermions in monolayer graphene and massive chiral fermions in bilayer graphene are distinctly different from the electron dynamics in traditional two-dimensional electron systems. In bilayer graphene, we described in detail about possible transitions from the fractional quantum Hall state to a compressible state and back to the FQHE state in the same Landau level by simply tuning the band gap at a given electron density. Similarly, we suggest the possibility of a FQHE—no-FQHE—FQHE transition within a Landau level of bilayer graphene. These controllable driven transitions are unique to bilayer graphene and do not exist in conventional 2D electron systems. Experimental observation of these will provide a rare glimpse into the properties of incompressible and compressible states in bilayer graphene. Incompressible states in trilayer graphene are also briefly discussed. Novel states, such as the incompressible Pfaffian state at $\nu = \frac{5}{2}$ are expected to be present in bilayer graphene. Finally, we present a brief description of the properties of FQHE states of Dirac fermions on the surface of a topological insulator.

References

1. K. von Klitzing, G. Dorda, M. Pepper, Phys. Rev. Lett. **45**, 494 (1980)
2. K. von Klitzing, Rev. Mod. Phys. **58**, 519 (1986)
3. H.L. Störmer, Physica B **177**, 401 (1992)
4. H.L. Störmer, Rev. Mod. Phys. **71**, 875 (1999)
5. R.B. Laughlin, Phys. Rev. Lett. **50**, 1395 (1983)
6. R.B. Laughlin, Rev. Mod. Phys. **71**, 863 (1999)
7. T. Chakraborty, P. Pietiläinen, *The Quantum Hall Effects*, 2nd edn. (Springer, New York, 1995)
8. S.M. Girvin, in *The Quantum Hall Effects: Poincarè Seminar 2004*, ed. by B. Ducot, B. Duplantier, V. Pasquier, E. Rivasseau (Birkhäuser, Basel, 2005), p. 133
9. R.B. Laughlin, *A Different Universe* (Basic Books, New York, 2005)
10. S. Das Sarma, A. Pinczuk (eds.), *Perspectives in Quantum Hall Effects* (Wiley, New York, 1997)
11. B.I. Halperin, Helv. Phys. Acta **56**, 75 (1983)

12. V.S. Khrapai, A.A. Shashkin, M.G. Trokina, V.T. Dolgopolov, V. Pellegrini, F. Beltram, G. Biasiol, L. Sorba, Phys. Rev. Lett. **100**, 196805 (2008)
13. B.I. Halperin, Phys. Rev. Lett. **52**, 1583 (1984)
14. T. Chakraborty, K. von Klitzing, Phys. Can. **67**(3), 161 (2011). arXiv:1102.5250
15. F.D.M. Haldane, in *The Quantum Hall Effect*, ed. by R.E. Prange, S.M. Girvin (Springer, New York, 1987), p. 303
16. F.D.M. Haldane, E.H. Rezayi, Phys. Rev. Lett. **54**, 237 (1985)
17. J.K. Jain, Phys. Rev. Lett. **63**, 199 (1989)
18. J.K. Jain, Phys. Rev. B **40**, 8079 (1989)
19. O. Heinonen (ed.), *Composite Fermions* (World Scientific, Singapore, 1998)
20. B.I. Halperin, in *Perspectives in Quantum Hall Effects*, ed. by S. Das Sarma, A. Pinczuk (Wiley, New York, 1997)
21. B.I. Halperin, Physica E **20**, 71 (2003)
22. R.L. Willett, Adv. Phys. **46**, 447 (1997)
23. K.S. Novoselov, Rev. Mod. Phys. **83**, 837 (2011)
24. A.K. Geim, Rev. Mod. Phys. **83**, 851 (2011)
25. A.K. Geim, K.S. Novoselov, Nat. Mater. **6**, 183 (2007)
26. T. Ando, A.B. Fowler, F. Stern, Rev. Mod. Phys. **54**, 437 (1982)
27. P.R. Wallace, Phys. Rev. **71**, 622 (1947)
28. T. Ando, Physica E **40**, 213 (2007)
29. K.S. Novoselov, Z. Jiang, Y. Zhang, S.V. Morozov, H.L. Stormer, U. Zeitler, J.C. Maan, G.S. Boebinger, P. Kim, A.K. Geim, Science **315**, 1379 (2007)
30. D.S.L. Abergel, V. Apalkov, J. Berashevich, K. Ziegler, T. Chakraborty, Adv. Phys. **59**, 261 (2010)
31. C. Beenakker, Rev. Mod. Phys. **80**, 1337 (2008)
32. V.P. Gusynin, V.A. Miransky, S.G. Sharapov, I.A. Shovkovy, Low Temp. Phys. **34**, 778 (2008)
33. V.P. Gusynin, S.G. Sharapov, J.P. Carbotte, Int. J. Mod. Phys. B **21**, 4611 (2007)
34. A.H. Castro Neto, F. Guinea, N.M.R. Peres, K.S. Novoselov, A.K. Geim, Rev. Mod. Phys. **81**, 109 (2009)
35. N.M.R. Peres, J. Phys. Condens. Matter **21**, 323201 (2009)
36. L.M. Malard, M.A. Pimenta, G. Dresselhaus, M.S. Dresselhaus, Phys. Rep. **473**, 51 (2009)
37. A.K. Geim, Science **324**, 1530 (2009)
38. N.J.M. Horing, Philos. Trans. R. Soc. Lond. A **368**, 5525 (2010)
39. Y.H. Wu, T. Yu, Z.X. Shen, J. Appl. Phys. **108**, 071301 (2010)
40. M. Orlita, M. Potemski, Semicond. Sci. Technol. **25**, 063001 (2010)
41. C. Soldano, A. Mahmood, E. Dujardin, Carbon **48**, 2127 (2010)
42. W. Choi, I. Lahiri, R. Seelaboyina, Y.S. Kang, Crit. Rev. Solid State Mater. Sci. **35**, 52 (2010)
43. C.N.R. Rao, A.K. Sood, R. Voggu, K.S. Subrahmanyam, J. Phys. Chem. Lett. **1**, 572 (2010)
44. Y. Zhu, S. Murali, W. Cai, X. Li, J.W. Suk, J.R. Potts, R.S. Ruoff, Adv. Mater. **22**, 3906 (2010)
45. M.J. Allen, V.C. Tung, R.B. Kaner, Chem. Rev. **110**, 132 (2010)
46. N.M.R. Peres, Rev. Mod. Phys. **82**, 2673 (2010)
47. S. Das Sarma, S. Adam, E.H. Hwang, E. Rossi, Rev. Mod. Phys. **83**, 407 (2011)
48. A.V. Rozhkov, G. Giavaras, Y.P. Bliokh, V. Freilikher, F. Nori, Phys. Rep. **503**, 77 (2011)
49. C.L. Kane, E.J. Mele, Phys. Rev. Lett. **95**, 226801 (2005)
50. X.F. Wang, T. Chakraborty, Phys. Rev. B **75**, 033408 (2007)
51. N.A. Sinitsyn et al., Phys. Rev. Lett. **97**, 106804 (2006)
52. L.D. Landau, E.M. Lifshitz, *Quantum Mechanics, Non-relativistic Theory*, 3rd edn. (Pergamon Press, New York, 1977)
53. A.J.M. Giesbers, U. Zeitler, M.I. Katsnelson, L.A. Ponomarenko, T.M. Mohiuddin, J.C. Maan, Phys. Rev. Lett. **99**, 206803 (2007)
54. V.M. Apalkov, T. Chakraborty, Phys. Rev. Lett. **97**, 126801 (2006)
55. M.O. Goerbig, R. Moessner, B. Ducot, Phys. Rev. B **74**, 161407(R) (2006)

56. V. Apalkov, X.F. Wang, T. Chakraborty, Int. J. Mod. Phys. B **21**, 1165 (2007)
57. F.D.M. Haldane, Phys. Rev. Lett. **51**, 605 (1983)
58. G. Fano, F. Ortolani, E. Colombo, Phys. Rev. B **34**, 2670 (1986)
59. M. Greiter, Phys. Rev. B **83**, 115129 (2011)
60. C. Toke, P.E. Lammert, V.H. Crespi, J.K. Jain, Phys. Rev. B **74**, 235417 (2006)
61. N. Shibata, K. Nomura, J. Phys. Soc. Jpn. **78**, 104708 (2009)
62. Z. Papic, M.O. Goerbig, N. Regnault, Phys. Rev. Lett. **105**, 176802 (2010)
63. C. Toke, J.K. Jain, Phys. Rev. B **75**, 245440 (2007)
64. K.S. Novoselov, A.K. Geim, S.V. Morozov, D. Jiang, M.I. Katsnelson, I.V. Grigorieva, S.V. Dubonos, A.A. Firsov, Nature **438**, 197 (2005)
65. Y. Zhang, Y.-W. Tan, H.L. Stormer, P. Kim, Nature **438**, 201 (2005)
66. K.I. Bolotin, K.J. Sikes, Z. Jiang, G. Fudenberg, J. Hone, P. Kim, H.L. Störmer, Solid State Commun. **146**, 351 (2008)
67. X. Du, I. Skachko, A. Barker, E. Andrei, Nat. Nanotechnol. **3**, 491 (2008)
68. X. Du, I. Skachko, F. Duerr, A. Luican, E.Y. Andrei, Nature **462**, 192 (2009)
69. D.A. Abanin, I. Skachko, X. Du, E.Y. Andrei, L.S. Levitov, Phys. Rev. B **81**, 115410 (2010)
70. K.I. Bolotin, F. Ghahari, M.D. Shulman, H.L. Störmer, P. Kim, Nature **462**, 196 (2009)
71. I. Skachko, X. Du, F. Duerr, A. Luican, D.A. Abanin, L.S. Levitov, E.Y. Andrei, Philos. Trans. R. Soc. Lond. A **368**, 5403 (2010)
72. H. Wang, D.N. Sheng, L. Sheng, F.D.M. Haldane, Phys. Rev. Lett. **100**, 116802 (2008)
73. G.S. Boebinger, A.M. Chang, H.L. Störmer, D.C. Tsui, Phys. Rev. Lett. **55**, 1606 (1985)
74. G. Ebert, K. von Klitzing, J.C. Maan, G. Remenyi, C. Probst, G. Weimann, W. Schlapp, J. Phys. C, Solid State Phys. **17**, L775 (1984)
75. D.C. Tsui, H.L. Störmer, J.C.M. Hwang, J.S. Brooks, M.J. Naughton, Phys. Rev. B **28**, 2274(R) (1983)
76. E.V. Kurganova, A.J.M. Giesbers, R.V. Gorbachev, A.K. Geim, K.S. Novoselov, J.C. Maan, U. Zeitler, Solid State Commun. **150**, 2209 (2010)
77. F. Ghahari, Y. Zhao, P. Cadden-Zimansky, K. Bolotin, P. Kim, Phys. Rev. Lett. **106**, 046801 (2011)
78. C.R. Dean, A.F. Young, P. Cadden-Zimansky, L. Wang, R. Hen, K. Watanabe, T. Taniguchi, P. Kim, J. Hone, K.L. Shepard, Nat. Phys. **7**, 693 (2011)
79. W. Bao, Z. Zhao, G. Liu, P. Kratz, L. Jing, J. Velasco Jr., D. Smirnov, C.N. Lau, Phys. Rev. Lett. **105**, 246601 (2010)
80. E. McCann, V.I. Fal'ko, Phys. Rev. Lett. **96**, 086805 (2006)
81. T. Chakraborty, V.M. Apalkov, Solid State Commun. (2013)
82. E. McCann, Phys. Rev. B **74**, 161403 (2006)
83. E.V. Castro, K.S. Novoselov, S.V. Morozov, N.M.R. Peres, J.M.B. Lopes dos santos, J. Nilsson, F. Guinea, A.K. Geim, A.H. Castro Neto, Phys. Rev. Lett. **99**, 216802 (2007)
84. M. Mucha-Kruczynski, D.S.L. Abergel, E. McCann, V.I. Fal'ko, J. Phys. Condens. Matter **21**, 344206 (2009)
85. J.M. Pereira Jr., F.M. Peeters, P. Vasilopoulos, Phys. Rev. B **76**, 115419 (2007)
86. V.M. Apalkov, T. Chakraborty, Phys. Rev. Lett. **105**, 036801 (2010)
87. C. Berger, J. Veuillen, L. Magaud, P. Mallet, V. Olevano, M. Orlita, P. Plochoka, C. Faugeras, G. Martinez, M. Potemski, C. Naud, L.P. Levy, D. Mayou, Int. J. Nanotechnol. **7**, 383 (2010)
88. A. Reina, X. Jia, J. Ho, D. Nezich, H. Son, V. Bulovic, M.S. Dresselhaus, J. Kong, Nano Lett. **9**, 30 (2009)
89. D.L. Miller, K.D. Kubista, G.M. Rutter, M. Ruan, W.A. de Heer, P.N. First, J.A. Stroscio, Science **324**, 924 (2009)
90. J. Hass, F. Varchon, J.E. Millan-Otoya, M. Sprinkle, N. Sharma, W.A. de Heer, C. Berger, P.N. First, L. Magaud, E.H. Conrad, Phys. Rev. Lett. **100**, 125504 (2008)
91. S. Latil, L. Henrard, Phys. Rev. Lett. **97**, 036803 (2006)
92. S. Shallcross, S. Sharma, O.A. Pankratov, Phys. Rev. Lett. **101**, 056803 (2008)
93. J.M.B. Lopes dos Santos, N.M.R. Peres, A.H. Castro Neto, Phys. Rev. Lett. **99**, 256802 (2007)

94. E.J. Mele, Phys. Rev. B **81**, 161405 (2010)

95. A. Luican, G. Li, A. Reina, J. Kong, R.R. Nair, K.S. Novoselov, A.K. Geim, E.Y. Andrei, Phys. Rev. Lett. **106**, 126802 (2011)

96. V.M. Apalkov, T. Chakraborty, Phys. Rev. B **84**, 033408 (2011)

97. T. Taychatanapat, K. Watanabe, T. Tanigushi, P. Jarillo-Herrero, Nat. Phys. **7**, 621 (2011)

98. A. Kumar, W. Escoffier, J.M. Poumirol, C. Faugeras, D.P. Arovas, M.M. Fogler, F. Guinea, S. Roche, M. Goiran, B. Raquet, Phys. Rev. Lett. **107**, 126806 (2011)

99. V.M. Apalkov, T. Chakraborty, Phys. Rev. B **86**, 035401 (2012)

100. S. Yuan, R. Roldan, M.I. Katsnelson, Phys. Rev. B **84**, 125455 (2011)

101. J.P. Eisenstein, in *Perspectives in Quantum Hall Effects*, ed. by S. Das Sarma, A. Pinczuk (Wiley-Interscience, New York, 1996), p. 37

102. R. Willett, J.P. Eisenstein, H.L. Störmer, D.C. Tsui, A.C. Gossard, J.E. English, Phys. Rev. Lett. **59**, 1776 (1987)

103. C. Zhang, T. Knuuttila, Y. Dai, R.R. Du, L.N. Pfeiffer, K.W. West, Phys. Rev. Lett. **104**, 166801 (2010)

104. N. Read, Physica B **298**, 121 (2001)

105. G. Moore, N. Read, Nucl. Phys. B **360**, 362 (1991)

106. M. Greiter, X.-G. Wen, F. Wilczek, Phys. Rev. Lett. **66**, 3205 (1991)

107. M. Greiter, X.-G. Wen, F. Wilczek, Nucl. Phys. B **374**, 567 (1992)

108. M. Levin, B.I. Halperin, B. Rosenow, Phys. Rev. Lett. **99**, 236806 (2007)

109. S.S. Lee, S. Ryu, C. Nayak, M.P.A. Fisher, Phys. Rev. Lett. **99**, 236807 (2007)

110. A. Stern, B.I. Halperin, Phys. Rev. Lett. **96**, 016802 (2006)

111. A. Stern, Ann. Phys. **323**, 204 (2008)

112. M. Dolev, M. Heiblum, V. Umansky, A. Stern, D. Mahalu, Nature **452**, 829 (2008)

113. V. Venkatchalam, A. Yacoby, L. Pfeiffer, K. West, Nature **469**, 185 (2011)

114. N. Read, D. Green, Phys. Rev. B **61**, 10267 (2000)

115. D.A. Ivanov, Phys. Rev. Lett. **86**, 268 (2001)

116. R.F. Service, Science **332**, 193 (2011)

117. M. Storni, R.H. Morf, S. Das Sarma, Phys. Rev. Lett. **104**, 076803 (2010)

118. M.R. Peterson, Th. Jolicoeur, S. Das Sarma, Phys. Rev. Lett. **101**, 016807 (2008)

119. N. Read, E. Rezayi, Phys. Rev. B **54**, 16864 (1996)

120. V. Apalkov, T. Chakraborty, Phys. Rev. Lett. **107**, 186803 (2011)

121. M.Z. Hasan, C.L. Kane, Rev. Mod. Phys. **82**, 3045 (2010)

122. X.-L. Qi, S.-C. Zhang, Phys. Today **63**, 33 (2010)

123. D. Hsieh, D. Qian, L. Wray, Y. Xia, Y.S. Hor, R.J. Cava, M.Z. Hasan, Nature (London) **452**, 970 (2008)

124. Y. Xia, D. Qian, D. Hsieh, L. Wray, A. Pal, H. Lin, A. Bansil, D. Grauer, Y.S. Hor, R.J. Cava, M.Z. Hasan, Nat. Phys. **5**, 398 (2009)

125. T. Hanaguri, K. Igarashi, M. Kawamura, H. Takagi, T. Sasagawa, Phys. Rev. B 081305(R) (2010)

126. P. Cheng, C. Song, T. Zhang, Y. Zhang, Y. Wang, J.-F. Jia, J. Wang, Y. Wang, B.-F. Zu, X. Chen, X. Ma, K. He, L. Wang, Z. Fang, X. Xie, X.-L. Qi, C.-X. Liu, S.-C. Zhang, Q.-K. Xue, Phys. Rev. Lett. **105**, 076801 (2010)

127. H. Zhang, C.-X. Liu, X.-L. Qi, X. Dai, Z. Fang, S.-C. Zhang, Nat. Phys. **5**, 438 (2009)

128. C.-X. Liu, X.-L. Qi, H.J. Zhang, X. Dai, Z. Fang, S.-C. Zhang, Phys. Rev. B **82**, 045122 (2010)

129. Z. Yang, J.H. Han, Phys. Rev. B **83**, 045415 (2011)

130. Z. Wang, Z.-G. Fu, S.-X. Wang, P. Zhang, Phys. Rev. B **82**, 085429 (2010)

131. V. Apalkov, T. Chakraborty, Phys. Rev. Lett. **107**, 186801 (2011)

132. G. Zhang, H. Qin, J. Teng, J. Guo, Q. Guo, X. Dai, Z. Fang, K. Wu, Appl. Phys. Lett. **95**, 053114 (2009)